Reflectance spectroradiometry applied to a semi-quantitative analysis of the mineralogy of the N4ws deposit, Carajás Mineral Province, Pará, Brazil

Elias Martins Guerra Prado [a,b], Adalene Moreira Silva [a], Diego Fernando Ducart [a], Catarina Labouré Bemfica Toledo [a], Luciano Mozer de Assis [c]

[a] Universidade de Brasília (UnB), Campus Darcy Ribeiro, Brasília, Brazil
[b] Serviço Geológico do Brasil (CPRM), Residência Rondônia (REPO), Porto Velho, Brazil
[c] Exploração Mineral de Ferrosos, Vale S.A., CTF - Miguelão, Fazenda Rio de Peixe, s/no, Nova Lima, MG, Brazil

ARTICLE INFO

ABSTRACT

Quantifying the abundance and physicochemical properties of minerals using reflectance spectroradiometry in the visible, near infrared and shortwave infrared (400–2500 nm) regions is an important tool in mineral exploration. In this study, the reflectance spectra of drill cores from the world-class N4WS iron deposit located in the Carajás Mineral Province, Brazil, were obtained. These spectra were validated using X-ray fluorescence (XRF) geochemical analyses and thin sections. The reflectance spectra were collected using a FieldSpec 3 spectroradiometer (ASD, Boulder, Colorado, USA) in 10 drill cores. The mineralogy of the deposit is mainly hematite, with lesser amounts of magnetite, goethite, quartz, kaolinite, gibbsite, smectite, talc, carbonate and chlorite. The mineralogy of the iron deposit was extracted from the spectral data using the geometry (depth and wavelength) of absorption features across the reflectance spectrum removed from the continuum. The depth of the absorption features is proportional to the mineral abundance, and the wavelength is proportional to the mineral chemical composition. The diagnostic absorption features of each mineral were used to determine the mineral abundance and composition. The final products include the abundance of iron (hydro) oxide (11.6% root-mean-square error [RMSE] Fe_2O_3); abundance of aluminous clays (RMSE 6% Al_2O_3); abundance of talc (8% RMSE MgO); identification of clay type (kaolinite, montmorillonite or gibbsite); composition of carbonate (dolomite vs. calcite); and composition of chlorite (Mg vs. Fe). The mineral abundance and composition results provided an effective characterisation of the ore, protore and host rocks and showed variations within the ore body.

© 2016 Elsevier B.V. All rights reserved.

1. Introduction

Reflectance spectroradiometry is a well-known and effective technique for identifying the mineralogy of mineral deposits in the different stages of mineral exploration, from prospection to production (Herrmann et al., 2001; Ducart et al., 2006; Harraden et al., 2013; Dalm et al., 2014). Spectral analyses of these deposits allows for a better understanding of mineralised areas that can provide additional information on the spatial distribution of minerals, assisting the identification of ore zones and associated contaminants. Analysis of absorption bands due to electronic transitions, vibrational modes, charge transfer, and other processes (e.g., see Hunt, 1977) is used for the mineral identification.

In addition to mineralogical mapping, spectral analyses can quantify the identified minerals, which may be performed by correlating spectral data with independent data, such as X-ray fluorescence (XRF) (Clark and Roush, 1984; Cudahy et al., 2009; Yang et al., 2011; Haest and Cudahy, 2012; Sonntag et al., 2012; Dai et al., 2013). This mineralogical characterisation could be affected by several factors, as for example, the

number and type of materials present, the weight fractions, the grain size of each material, and the viewing geometry (Clark and Roush, 1984). Quantitative analyses of the mineralogy of a rock through reflectance spectroradiometry require the following assumptions: (1) measured electromagnetic energy travels the same distance during its trajectory from light source to sample and from sample to sensor through a fixed measurement geometry (cf. Clark and Roush, 1984); (2) absorption intensity of a particular mineral in relation to the background (usually considered the continuum of the spectrum) is a function of the absorption coefficient and abundance of a mineral; thus, when the mineral is identified, its abundance may be determined by the absorption intensity (Hunt and Ashley, 1979; Clark and Roush, 1984); (3) crystal chemistry of a particular mineral determines the wavelength of its diagnostic absorption feature (cf. Hunt and Salisbury, 1971; Clark et al., 1990; Cudahy and Ramanaidou, 1997); and (4) scattering (crystal orientation, size/distribution/particle orientation) is isotropic (cf. Adams and Filice, 1967; Clark and Roush, 1984; Morris et al., 1985).

The main goal of this study is to use reflectance spectroradiometry to explore the N4WS iron deposit located in the Carajás Mineral Province, Pará, Brazil. For this purpose, a spectral study of nine drill holes distributed in three sections across the N4WS deposit was conducted and the results were integrated with geological and geochemical data collected over the same section. The results were used to perform qualitative and quantitative modelling of the mineralogy of the deposit.

1.1. Regional geology

The Carajás Mineral Province is located in the oldest part of the Amazonian Craton of Archean/Paleoproterozoic age (Gibbs et al., 1986; Machado et al., 1991). The region is dominated by metamorphosed volcano-sedimentary sequences and granitoids formed between 2.76 and 2.68 Ga as well as by the Pium and Xingu Mesoarchean complexes (Cordani et al., 1979; Tassinari, 1996; Santos, 2003; Santos et al., 2000, 2006; Tassinari and Macambira, 1999, 2004; Tassinari et al., 2000). The province comprises the Mesoarchean granite-greenstone terranes of Rio Maria South Domain, and the Neoarchean volcano-sedimentary sequences and granitoids of Carajás North Domain (Tassinari, 1996; Bizzi et al., 2003).

The tonalite-trondhjemite-granodiorite (TTG) terranes of the Xingu complex (2.86 Ga; Silva et al., 1974) form the base of the volcano-sedimentary sequence represented by the Itacaiúnas Supergroup. Granites and mafic-ultramafic units with ages ranging from 2.76 to 2.74 Ga intrude these sequences (Fig. 1).
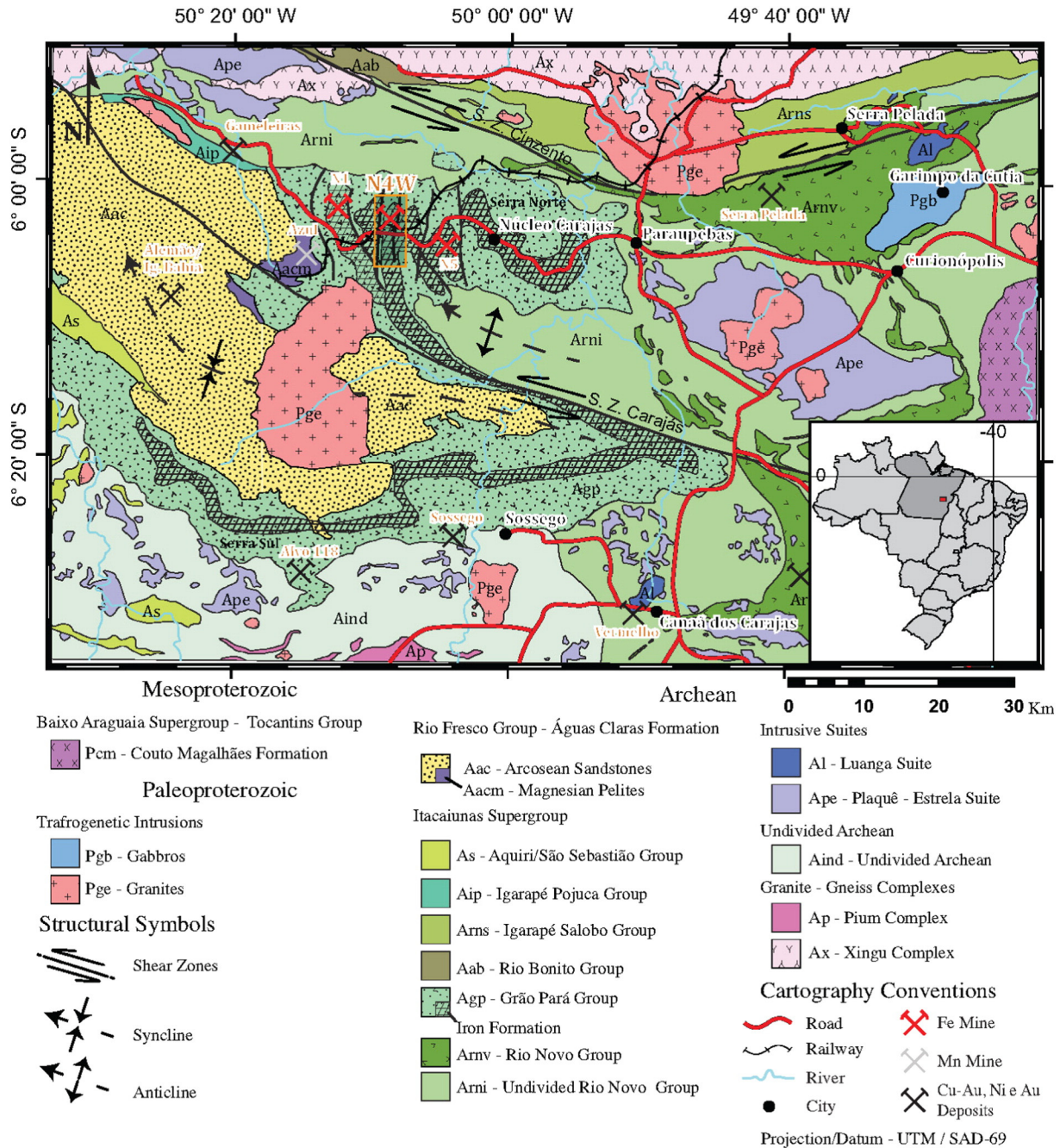

Fig. 1. Location map of the Carajás Mineral Province (Rosière et al., 2006) showing the major mineral deposits, including the iron deposits N1, N4 and N5 (Serra Norte), Serra Sul and Serra Leste; IOCG deposits (Alemão/Igarapé Bahia, Sossego, Cristalino); Cu—Au (W-Bi-Sn) deposits, such as Gamelera and Alvo 118; gold-platinum-palladium deposit of Serra Pelada; Azul manganese deposit and Vermelho nickel deposit.
Adapted from Silva and Hagemann (2013).

The Serra dos Carajás is an S-shaped hill composed of metamorphosed volcano-sedimentary rocks of the Grão Pará group (2.7 Ga), including the Carajás Formation that consists of jaspillites, which host iron mineralisation (Fig. 1).

The Parauapebas Formation constitutes the base of the Grão Pará Group and is represented by basalts, basaltic andesites and basic to intermediate pyroclastic rocks in smaller amounts (Krymsky et al., 2002; Lobato et al., 2005a; Meirelles et al., 1984), which occur concurrently beneath the Carajás Formation and reflect the contemporaneity of the two formations (Beisiegel et al., 1973; Macambira, 2003). These rocks are covered with banded iron formations (BIFs) and basic tuffs.

The Carajás Formation represents the intermediate portion of the Grão Pará Group (DOCEGEO, 1988) and contains layers and discontinuous lenses of Jaspilites and iron ore intruded by sills and mafic dikes. The Jaspilites have centimetre-thick intercalations of iron oxide, jasper and chert and are heavily weathered, with textures and primary structures preserved only at great depths. BIFs that include dolomite are also found (Macambira and Schrank, 2002; Dalstra and Guedes, 2004) and interpreted by Dalstra and Guedes (2004) as a carbonate facies of the BIF; however, a hydrothermal origin for this carbonate was suggested by Figueiredo e Silva et al. (2008).

The Igarapé Cigarra Formation is at the top of the Grão Pará Group and consists of mafic flows interlayered with tuffs followed by clastic sedimentary rocks, such as sillites, phyllites and greywackes (Gibbs et al., 1986; Macambira, 2003). The basalts with preserved igneous textures are the most common lithotypes (Macambira, 2003). Contact between this formation and the Carajás Formation is still uncertain, although it may be stratigraphic or structural, which calls into doubt their stratigraphic importance (Meirelles and Dardenne, 1991; Lindenmayer et al., 2001).

Psammo-pelitic rocks, such as arenites, calcarenites, siltites and conglomerates of the Águas Claras Formation, overlay the rocks of the Grão Pará Group (Fig. 1). The ages obtained from mafic dikes that cut these sedimentary rocks indicate that the deposition of sediments occurred at 2708 ± 37 Ma (Mougeot, 1996).

Type-A alkaline to sub-alkaline granites of Paleoproterozoic age, such as the Serra dos Carajás granite, intrude the Itacaiúnas Supergroup and have been dated at 1880 ± 2 Ma (Machado et al., 1991; Fig. 1). These granites are classified as oxidised magnetite-series rapakivi intrusions (Dall'Agnoll and de Oliveira, 2007).

The genesis of the iron ores of the Carajás Mineral Province as represented by the compact and friable hematite of the Carajás Formation is widely discussed in the literature, and three models have been proposed: supergene, hypogene and modified hypogene.

Tolbert et al. (1971) and Dardenne and Schobbenhaus (2001) proposed that the iron oxide enrichment of the ore bodies was residual and resulted from the supergene leaching of quartz and carbonate caused by meteoric waters during the lateritic alteration of the iron formations.

A different origin was proposed by Beisiegel et al. (1973), who suggested a hypogene model for the compact hematites, which indicated that hydrothermal fluids caused the metasomatic replacement of quartz. For the friable hematite, the authors proposed supergene enrichment. The role of hydrothermal fluids in iron mineralisation was also suggested by Dalstra and Guedes (2004); Rosière et al. (2004, 2005) and Lobato et al. (2005a, 2005b). For Rosière et al. (2004, 2005), structural control was observed in these mineralisations because fluid migration in these systems is controlled by areas of higher permeability, thus explaining the location of the ore bodies in the hinge zone of the Carajás synform.

The model advocated by Beisiegel et al. (1973) and Beukes et al. (2002) proposed that the genesis of the ore was associated with the supergene enrichment of areas previously altered by hypogene fluids, thus allowing the development of extensive layers of friable hematite in lateritic profiles that reach 500 m in depth. Tabular bodies of compact hematite occurred in association with friable ore and predominantly in the lower portion of the iron formation, whereas smaller lenticular bodies predominated at the top of the sequence.

1.2. Lithotypes of the N4WS deposit

The plateaus where the iron formations occur were mapped in detail at a scale of 1:20,000. The mapping data are the product of the final reports of the research conducted by Tolbert et al. (1971) and Resende and A.L.M. (1972)and updated from Macambira (2003), which focused on the iron formations and their host rocks. Fig. 2 shows the geological map of the N4WS deposit and is restricted to the plateau where the iron formations occur.

During the description of the cores and detailed mapping, which was performed by Vale S.A., 14 lithotypes were discriminated (Fig. 3; Tables 6–1: most common lithotypes in Serra Norte and their main characteristics; Assis, 2013), and the following six were described in the drill cores analysed in this study.

Ore "canga" (*OC*): lateritic cover that forms on the ore outcrops in situ. The thickness can reach over 20 m, and it has high Fe content and relatively low contaminants, enabling its potential use as ore. The main minerals are hematite and Goethite, with subordinate kaolinite. This lithotype is an indicator of iron ore occurrences.

Chemical "canga" (*CC*): derived from the regolith of mafic rocks or associated with mature and cemented colluvial deposits; also known as barren lateritic cover. Composed of hematite, goethite, gibbsite, kaolinite and talc.

Jaspilite (*JP*): banded iron formation composed of hematite and quartz that can be found with centimetre- to millimetre-thick laminations or an anastomosing pattern. Occasionally, the laminations alternate between mafic rock and jasper/chert. Breccias with jasper fragments encompassed by a magnetite-rich matrix also occur, commonly with veinlets of quartz and/or carbonate. Constant variation in size between magnetite and martite crystals is observed. It represents the protore in the region and has Fe content ranging between 20 and 40%.

Friable hematite (*FH*): iron ore with an average Fe content of 66%. Highly friable and porous Jaspilite structure partially to totally obliterated because of silica leaching. Colour varies from shades of grey to yellowish, which is associated with aluminum contamination. It is composed mainly of hematite, with subordinate goethite.

Unweathered mafic (*UM*): basalts, gabbros and diabases that show little to no weathering. Tuffs of pyroclastic rocks are also described but rare. Mafic rocks are systematically chloritized and locally rich in talc. Green to dark green, sometimes with typical volcanic structures, such as tonsils filled with quartz, carbonates and chlorites and possibly sulphides. These lithotypes occur either as flows or intruded in JPs in the form of sills and dykes;

Semi-decomposed mafic (*SDM*): saprolite of mafic rocks with relicts of the original protolith framework or total loss of the original structure.

2. Method

2.1. Sampling and spectral data measurement

The samples were collected from cores of nine drill holes over three E-W trending sections across the N4WS deposit. Representative samples of 15 cm were collected every 2 m (1766 samples), and half of each sample was separated for geochemical analysis (XRF). Certain samples were selected to produce thin sections to validate the minerals identified by spectral analysis. Magnetic susceptibility data obtained by Ferreira (2014) were incorporated in this study.

The reflectance spectrum of the samples was measured using the reflectance spectroradiometer FieldSpec3 Hi-Res® (ASD Inc., Boulder, Colorado, USA; 5111 measurements). The measurements were performed using the contact probe with the internal halogen lamp as the light source. The acquisition window of the contact probe has an
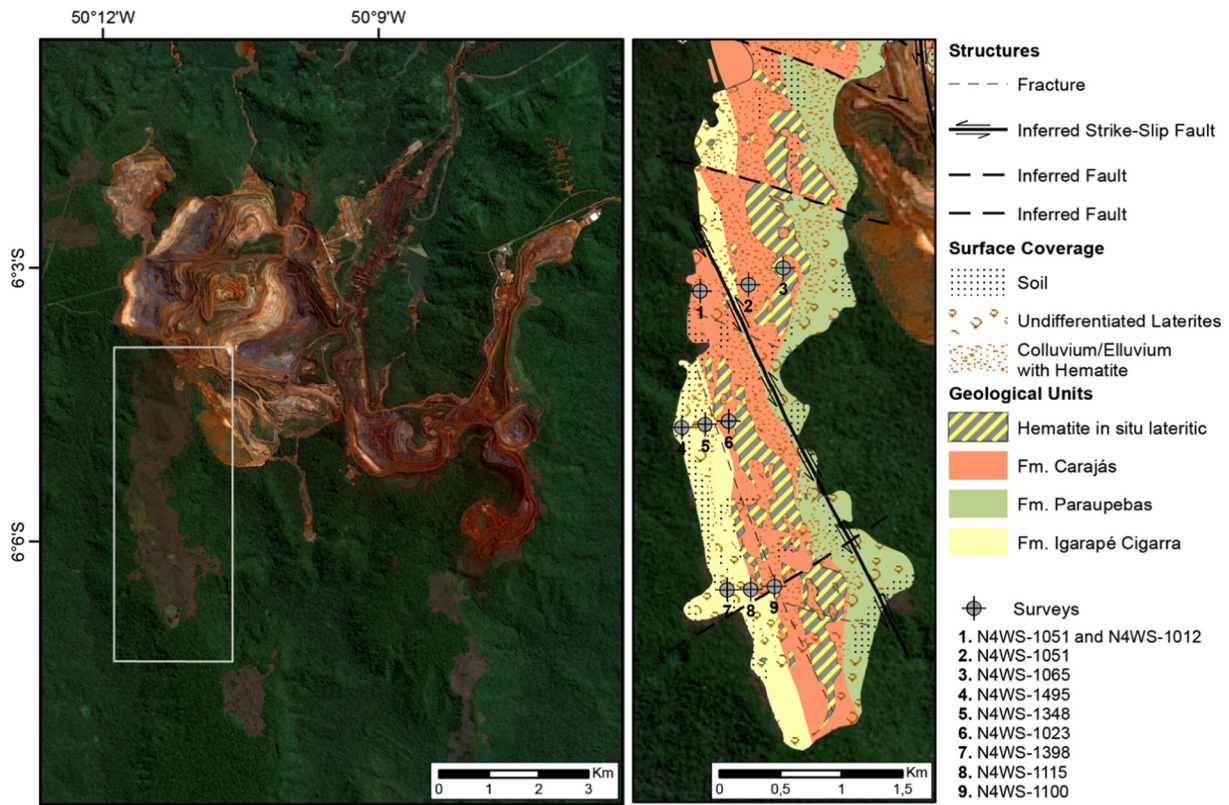
Fig. 2. Landsat 8 Operational Land Imager (OLI) image on the left showing the open pit of the N4 mine; the N4WS body is highlighted. On the right is the geological map of the N4WS body, focusing on the lithotypes described in the Serra Norte plateaus (Tolbert et al., 1971; Resende and A.L.M., 1972; Macambira, 2003). The studied drill holes are shown on the map and indicate the direction of the section.
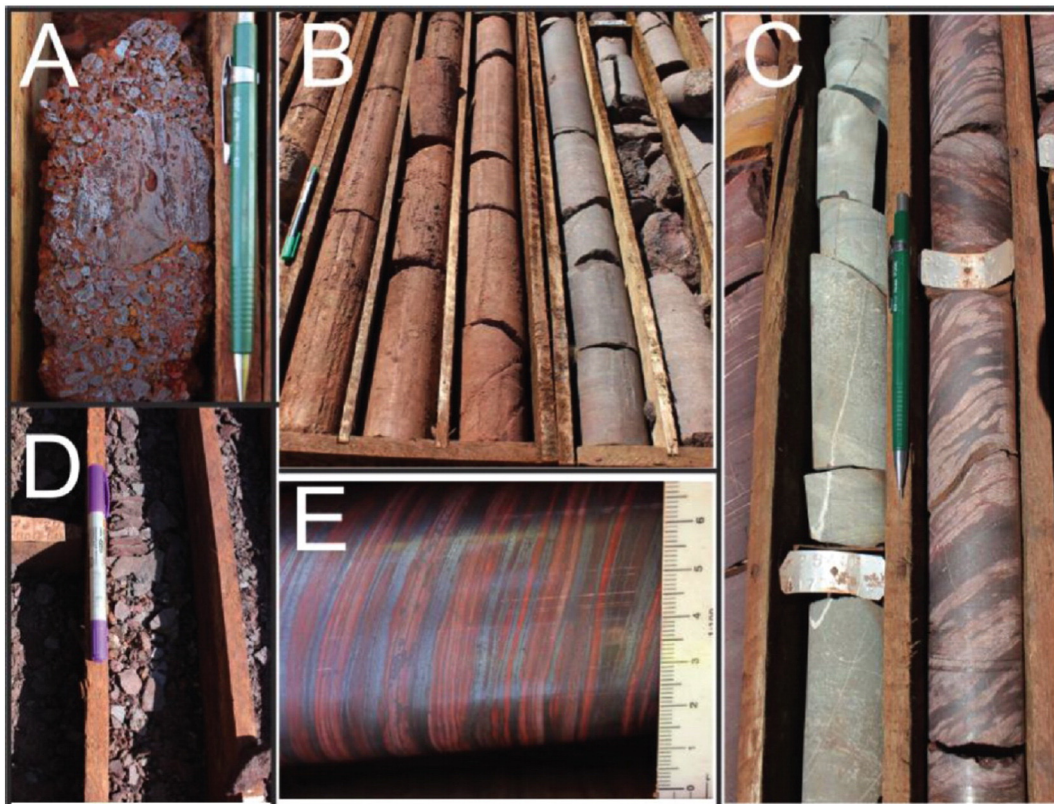

Fig. 3. Main lithotypes of the project area. A) Ore "canga" (OC). B) Chemical "canga" (CC) on the left and semi-decomposed mafic (SDM) on the right. C) Unweathered mafic (UM) on the left and jaspilite (JP) on the right. D) Friable hematite (FH). E) Details of the jaspilite (JP) banding showing intercalation of iron oxide and jasper bands.

area of 1 cm^2. The saved spectrum was the mean of 75 spectra measured in the same area.

The device collects the spectra in three modules: one that covers wavelengths from visible to near-infrared (VNIR: 350–1000 nm) and two that cover the short-wave infrared (SWIR: 1000–2500 nm). The sampling interval of the spectrometer is 1.4 nm in the VNIR and 2.0 nm in the SWIR, with a wavelength accuracy of ± 0.5 nm. The spectral resolution is 3 nm in the VNIR and 8 nm in the SWIR. The spectra collected by the spectral radiometer are converted from radiation to reflectance using the Spectralon™ signal. Device calibration was performed every 15 min during data collection. A 40 min warm up of the spectroradiometer was carried out before the measurements. The contact probe was cleaned after every measurement.

The quantitative analysis of spectral data is a technique that has been utilized for a number of years. In general, studies using the technique to quantify iron oxides of soils apply diffuse reflectance spectroscopy (Fernandes et al., 2004; Carioca et al., 2011; Gonçalves et al., 2012; Jiang et al., 2013), whereas studies where the technique is used to quantify the mineralogy of rock samples apply portable bi-directional reflectance spectroscopy (e.g., ASD-Fieldspec PIMA; Yang et al., 2011; Sonntag et al., 2012). Fernandes et al. (2009)suggested that laboratory bi-directional reflectance spectroscopy is as useful as diffuse reflectance spectroscopy to characterize soil iron oxides. Bi-directional reflectance spectroscopy is also used by robotic systems (e.g., HyLogger System; Cudahy et al., 2009), or by hyperspectral drill core scanners (Ross et al., 2013). This study uses a portable reflectance spectroradiometer (ASD FieldSpec) that includes two sensor heads for data collection: pistol grip or contact probe. The pistol grip requires an external light source for data collection; thus, the positioning configuration (distance, angle and height) of the pistol grip (sensor), light source and sample should be set for the specific measurements to be performed. The contact probe has internal illumination, and the data are collected with the probe in direct contact with the sample. The fixed geometry of illumination angle and sensor and the fixed distance between light source, sample and sensor makes the contact probe the most suitable sensor head configuration for this study.

2.2. Analysis of spectral data

When light interacts with a mineral or rock, it is preferably absorbed at certain wavelengths, whereas it is transmitted at other wavelengths. Reflectance is defined as the ratio between the intensity of the light reflected by the sample and intensity of the incident light (Van der Meer, 2004). Electronic transition and charge transfer processes (e.g., change in the electronic state of electrons bound to atoms or molecules) associated with transition metal ions such as Fe, Ti, Cr, etc. determine the position of the diagnostic spectral absorption features of certain minerals in the VNIR regions to a large extent (Hunt, 1977; Adams, 1974, 1975; Burns, 1993). Vibration processes related to H_2O, OH^- and CO_3 also produce characteristic absorption features in the SWIR region (Hunt, 1977).

The position, shape and depth of these absorption features are controlled by the crystal structure and chemical composition of the

minerals. Therefore, variables that characterize these absorption features (spectral parameters) can be directly correlated to the chemical composition and crystal structure of the sample (Van der Meer, 2004). The spectral parameters were obtained from the polynomial curve that best fits the reflectance spectrum for which the continuum was removed (Fig. 4). The polynomial fit approach to the spectral feature smoothes out some of the effects of noise in the data and is not affected by overall band shape (Cloutis et al., 1986). Mathematically, the continuum removed spectrum is obtained by the following equation (Clark et al., 2003):

$$L_c(w) = L(w)/C_1(w)$$

where $L(w)$ is the reflectance spectrum, $C_1(w)$ is the continuum to the reflectance spectrum and $L_c(w)$ is the continuum removed spectrum.

The position of the absorption feature is defined as the wavelength at which the absorption feature reaches the reflectance minimum of the curve, and the position of a reflectance feature is defined as the wavelength at which the feature reaches the reflectance maximum of the curve. The depth of the absorption feature was calculated using the method of Clark and Roush (1984) by subtracting the minimum reflectance value of the polynomial curve from the reflectance value of the continuum at the same wavelength and then dividing this value by the reflectance of the continuum. When the absorption feature is not present in the analysed spectrum, the depth value is equal or close to zero, indicating the absence of the investigated mineral. The asymmetry factor of the feature is defined by Van der Meer (2004) as the ratio of the areas on the right and left of the wavelength of minimum reflectance. The slope of a given region of the spectrum is calculated by obtaining the slope of the line tangent to this region (Fig. 4).

Data were analysed using the commercial software "The Spectral Geologist" (TSG Core™, CSIRO Earth Science and Resource Engineering - CESRE - Division, Sydney, Australia), which was used to process the spectral reflectance data, obtain the spectral parameters and extract the mineral abundance, composition and crystallinity data. First, the spectral parameters of individual absorption features, such as the depth, wavelength or ratio between spectral bands (Table 1), were calculated and then integrated to generate the abundance, composition and crystallinity data of the minerals (Table 2). In addition to the spectral parameters developed in this study, certain parameters were based on those proposed by Haest and Cudahy (2012)and adapted to the project.

Iron oxides produce characteristic absorption features in the VNIR (Hunt and Ashley, 1979; Morris et al., 1985; Sherman and Waite, 1985; Cudahy and Ramanaidou, 1992, 1997). These absorption features are caused by electronic processes involving Fe^{3+} bonded to an octahedral site by oxygen ligands (hematite) or oxygen and hydroxyl ligands (goethite). Electronic processes include the (1) transition of electrons to an upper energy level within unfilled orbitals (crystal field absorption), (2) transfer of charge between metals and ligands (charge transfer absorption), and (3) transitions resulting from the interaction between adjacent Fe^{2+} cations (Sherman and Waite, 1985). Goethite
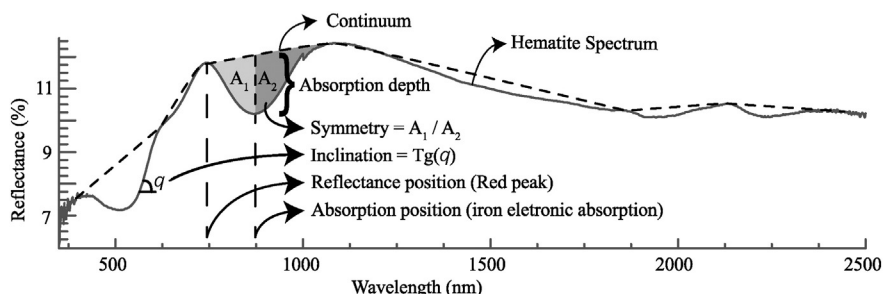

Fig. 4. Spectral parameters obtained from the mean spectra of each sample collected in this study.

Table 1
Algorithms for the extraction of spectral data (band ratio, absorption depth, minimum absorption wavelength, etc.) of individual absorption features.

Parameter	Function	TSG core algorithm
600_700SL	Identify Fe (hydro-)oxides	PFIT: Continuum slope ranging between 600 and 740 nm
900D	Identify and quantify Fe (hydro-)oxides	PFIT: Depth of the continuum removed spectrum calculated using a fifth-degree polynomial from 750 to 1250 nm, with a focus ranging between 800 and 1020 nm
900Wvl	Differentiate hematite-goethite	PFIT: Wavelength of the continuum removed spectrum calculated using a fourth-degree polynomial from 750 to 1050 nm, with a focus ranging between 800 and 1020 nm
N1650R	Albedo	PROFILE: Mean reflectance at 1650 ± 100 nm
2160D2190	Differentiate kaolin-group minerals from other Al phyllosilicates (e.g., aluminous smectite)	ARITH: (R2136 + R2188)/(R2241 + R2171)
$2200D_K$	Identify and quantify kaolinite	PFIT: Depth of the continuum removed spectrum calculated using a twelfth-degree polynomial from 2230 to 2245 nm, with a focus ranging between 2200 and 2215 nm
2170SL	Kaolinite crystallinity index	ARITH: R2180/R2166
$2200D_S$	Identify and quantify smectite	PFIT: Depth of the continuum removed spectrum calculated using a tenth-degree polynomial from 2150 to 2267 nm, with a focus ranging between 2193 and 2225 nm
2260D	Identify and quantify gibbsite	PFIT: Depth of the continuum removed spectrum calculated using a twelfth-degree polynomial from 2115 to 2475 nm, with a focus ranging between 2235 and 2300 nm
1450D	Identify gibbsite	PFIT: Depth of the continuum removed spectrum calculated using a twelfth-degree polynomial from 1350 to 1710 nm, with a focus ranging between 1430 and 1467 nm
1400D	Identify talc and kaolinite	PFIT: Depth of the continuum removed spectrum calculated using an eighth-degree polynomial from 1380 to 1460 nm, with a focus ranging between 1390 and 1420 nm
2380D	Identify talc	ARITH: (R2365 + R2415)/(R2381 + R2390)
2310D	Identify and quantify talc	PFIT: Depth of the continuum removed spectrum calculated using a twelfth-degree polynomial from 2242 to 2342 nm, with a focus ranging between 2305 and 2320 nm
1500SL	Identify Fe^{2+}	ARITH: (R1650/R1350)
2250D	Identify chlorite	ARITH: (R2227 + R2275)/R2241 + R2259)
2335D	Identify and quantify chlorite	PFIT: Depth of the continuum removed spectrum calculated using a twelfth-degree polynomial from 2171 to 2439 nm, with a focus ranging between 2300 and 2379 nm
2335Wvl	Chlorite composition	PFIT: Wavelength of the continuum removed spectrum calculated using a tenth-order polynomial from 2272 to 2381 nm, with a focus ranging between 2310 and 2370 nm
2330D	Identify and quantify carbonates	PFIT: Depth of the continuum removed spectrum calculated using a tenth-order polynomial from 2250 to 2360 nm, with focus ranging between 2310 and 2345 nm
2330De	Identify carbonates	ARITH: (R2265 + R2349)/(R2316 + R2333)
2330Wvl	Carbonate composition	PFIT: Wavelength of the continuum removed spectrum calculated using a tenth-order polynomial from 2300 to 2360 nm
2330Asym	Identify carbonates	PFIT: Simetry of the continuum removed spectrum calculated using a eight-order polynomial from 2120 to 2370 nm, with focus ranging between 2235 and 2370 nm

and hematite have characteristic crystal field absorptions between 630 and 715 nm and 850–1000 nm and an absorption feature caused by charge transfers between 480 and 550 nm (Fig. 5; Curtiss, 1985; Morris et al., 1985). Hunt and Ashley (1979) observed that the abundance of iron (hydro-)oxides is related to the depth of the absorption generated by the crystal field between 850 and 1000 nm, which was confirmed by Cudahy and Ramanaidou (1992). Haest and Cudahy (2012) observed that the depth of this absorption feature is influenced by the albedo of the sample; thus, two samples with the same amount of iron may have different depths of absorption if one is darker than the other.

The identification of iron (hydro-)oxide in the spectrum was performed using the slope of the spectral curve from 600 to 740 nm (600_740SL, Table 1). The iron (hydro-)oxide has a positive slope in this region of the spectrum because of absorption of crystal field from 630 to 715 nm (Fig. 5). The depth of the absorption feature from 850 to 1000 nm was calculated for the samples with the index 600_740SL > 0, was based on a fifth-degree polynomial, fitted to the continuum removed spectrum from 750 to 1250 nm with a focus ranging between 800 and 1020 nm (900D, Tables 1 and 2). To address the influence of albedo, a spectral index was created based on the mean reflectance at 1650 ± 100 nm (N1650R, Table 1; Haest and Cudahy, 2012).

The position of the absorption feature from 850 to 1000 nm in the iron (hydro-)oxides is a function of its composition (Fig. 5; Townsend, 1987; Cudahy and Ramanaidou, 1997). Townsend (1987) observed that the position of the feature varies from ~860 nm for pure hematite samples to ~920 nm for pure goethite samples. These absorptions were determined visually from spectra without continuum removal and thus the actual position of the minimum is modified by a slope effect related to the background continuum. Haest and Cudahy (2012) observed that when this background slope effect is normalized out,

the wavelength position of hematite and goethite ranges from ~880 nm for pure hematite to ~960 nm for pure goethite. The wavelength of the feature position was calculated from a fourth-degree polynomial, fitted to the continuum removed reflectance spectrum from 750 to 1050 nm, with a focus ranging between 800 and 1020 nm (900Wvl, Tables 1 and 2).

Hunt and Salisbury (1970) observed that a broad absorption feature centred at 1100 nm has a depth proportional to the Fe^{2+} content. The abundance of Fe^{2+} was obtained from the slope of the spectral curve between 1350 and 1650 nm (1500SL, Table 4.1).

Phyllosilicates and carbonates have characteristic absorption features in the SWIR region related to bonds between H_2O molecules, metal-OH and CO_3^{2-}. In this study, absorption features related to Al—OH bonds, which occur in the kaolin-group minerals, smectite and gibbsite, Mg—OH bonds, which occur in chlorites and talc, and CO_3, which occurs in carbonates, were used to extract estimates of the relative mineral abundance and composition. The minerals containing Al—OH in their structure have characteristic absorption features ranging between 2185 and 2210 nm in continuum removed spectra (Clark et al., 1990). The depth of these absorption features was used in this study to determine the abundance of these minerals. The various minerals that have Al—OH in their structure were differentiated by the presence or absence of characteristic absorption features between 2160 and 2350 nm in continuum removed spectra, and three parameters were observed: abundance of kaolinite, abundance of smectite, and abundance of gibbsite (Table 2). Some factors could complicate the relation between absorption depth and mineral abundance, or between band position and chemical composition. For example, additional Al—OH minerals present in the same sample have absorptions in the same position. In consequence, they will affect the depth of the Al—OH absorption. The abundance of a specific aluminous phyllosilicate in samples with a mixture of aluminous phyllosilicates cannot be accurately

Table 2
Spectral products applied in this study to extract the mineral abundance and compositional data of the N4WS drill cores.

Name	Detected minerals	Base algorithm	Filters/masks	Correlation trend
Abundance of Fe-(hydro-) oxides	Hematite, goethite	900D	$900D \geq 0.025$ $600\_740SL > 0$ Chlorite, kaolinite, gibbsite, Al-smectite, talc and carbonate abundance $= 0$	$\% Fe_2O_3 = 130.83 \times (900D) + 27.679$ Accuracy: 11.6% Fe_2O_3 total
Hematite-goethite distribution	Hematite/goethite ratio	900Wvl	$600\_740SL > 0$	
Abundance of kaolinite	Kaolinite	$2200D_K$	$2200D_K \geq 0.02$ $2160D2190 > 0.001$ Gibbsite, Al-smectite abundance $= 0$	$\% Al_2O_3 = 69.543 \times (2200D_K) + 9.8152$ Accuracy: 6% Al_2O_3
Crystallinity of kaolinite	Kaolinite	$2170SL + 2200D_K$	$2200D_K \geq 0.02$ $2160D2190 > 0.001$ Gibbsite, Al-smectite abundance $= 0$	
Abundance of Al-smectite	Al-smectite	$2200D_S$	$2200D_S \geq 0.006$ $2160D2190 < 0.001$ $1400D > 0.0039$ Gibbsite abundance $= 0$	
Abundance of gibbsite (gib_abun)	Gibbsite	2260D	$2260D > 0.009$ $1450 > 0.011$	$\% Al_2O_3 = 139.67 \times (2260D) + 7.1136$ Accuracy $= 10\%$ Al_2O_3
Abundance of talc	Talc	2310D	$2310D > 0.02$ $1400D > 0.0039$ $2380D > 1$ Carbonate and chlorite abundance $= 0$	$\% MgO = 24.354 \times (2310D) + 3.7029$ Accuracy: 8% MgO
Abundance of chlorite	Chlorite	2335D	$2335D > 0.02$ $2250D > 1$ Gibbsite, carbonate and talc abundance $= 0$	
Composition of chlorite	Chlorite	2335Wvl	$2335D > 0.02$ $2250D > 1$ Gibbsite, carbonate and talc abundance $= 0$	
Abundance of carbonate	Calcite, dolomite	2330D	$2330D \geq 0.007$ $2330De > 1.003$ $2330Asym > 1.11$ $2250D < 1.004$ $2380D < 1$ Chlorite and talc abund. $= 0$	$\% MgO + \% CaO = 74.948 * (2330D) + 1.6862$ Accuracy: 7% (%MgO + %CaO)
Composition of carbonate	Calcite, dolomite	2330Wvl	$2330D \geq 0.007$ $2330De > 1.003$ $2330Asym > 1.11$ $2250D < 1.004$ $2380D < 1$ Chlorite and talc abund. $= 0$	

determined with the approach applied in this manuscript, which only provides the abundance of the "spectrally" dominant phyllosilicate, thus limiting the quantitative character of the result. To address this
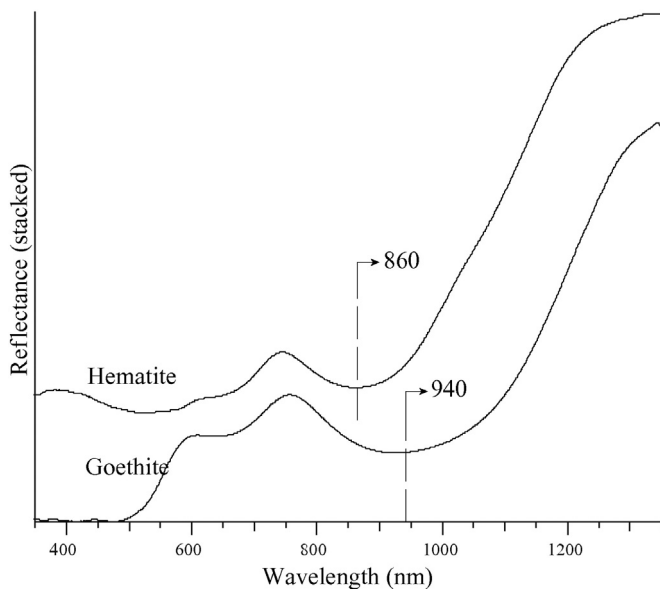

Fig. 5. Reflectance spectra of hematite and goethite; the position of the absorption feature of these minerals is highlighted.

issue, some filters were created to detect these mixtures, and then, samples with mixtures were discarded.

Kaolin-group minerals have a dominant absorption feature set at 2208 ± 3 nm in continuum removed spectra that is produced by Al—OH bonds (Fig. 6; Crowley and Vergo, 1988; Clark et al., 1990; Cudahy, 1997; Bishop et al., 2008). All kaolin-group minerals are characterised by additional absorption features between 2160 and 2190 nm in continuum removed spectra, which are also produced by Al—OH bonds (Clark et al., 1990; Cudahy, 1997). The distinction between the various minerals of this group is based on the position and depth of these additional absorption features. Kaolinite has an absorption feature near 2160 nm in continuum removed spectra (Clark et al., 1990; Cudahy, 1997) that is more pronounced in kaolinites with increased crystallinity (structural order; Fig. 6). A ratio of four bands was used to test the intensity of the absorption feature from 2160 to 2180 nm and differentiate the kaolin-group minerals from other aluminous phyllosilicates (Cudahy et al., 2008; 2160D2190, Table 1) using the condition 2160D2190 > 0.001. The kaolinite crystallinity was obtained from the ratio of the reflectance at 2180 nm and 2166 nm plus the depth of the absorption feature at 2208 nm ($2170SL + 2200D_K$, Table 1 and Table 2; Senna et al., 2008). The term "kaolinite cristallinity" is referred here as the estimation of octahedral vacancy (structural) disorder in kaolinite. The abundance of kaolinite was obtained from the calculation of the depth of the absorption feature at 2208 nm using a twelfth-degree polynomial fitted to the continuum removed spectrum between 2130 and 2245 nm, with the focus ranging between 2200 and 2215 nm (2200Dk, Table 1 and Table 2; Haest and Cudahy, 2012). Also, the algorithm discarded mixtures with Al-smectite and gibbsite.
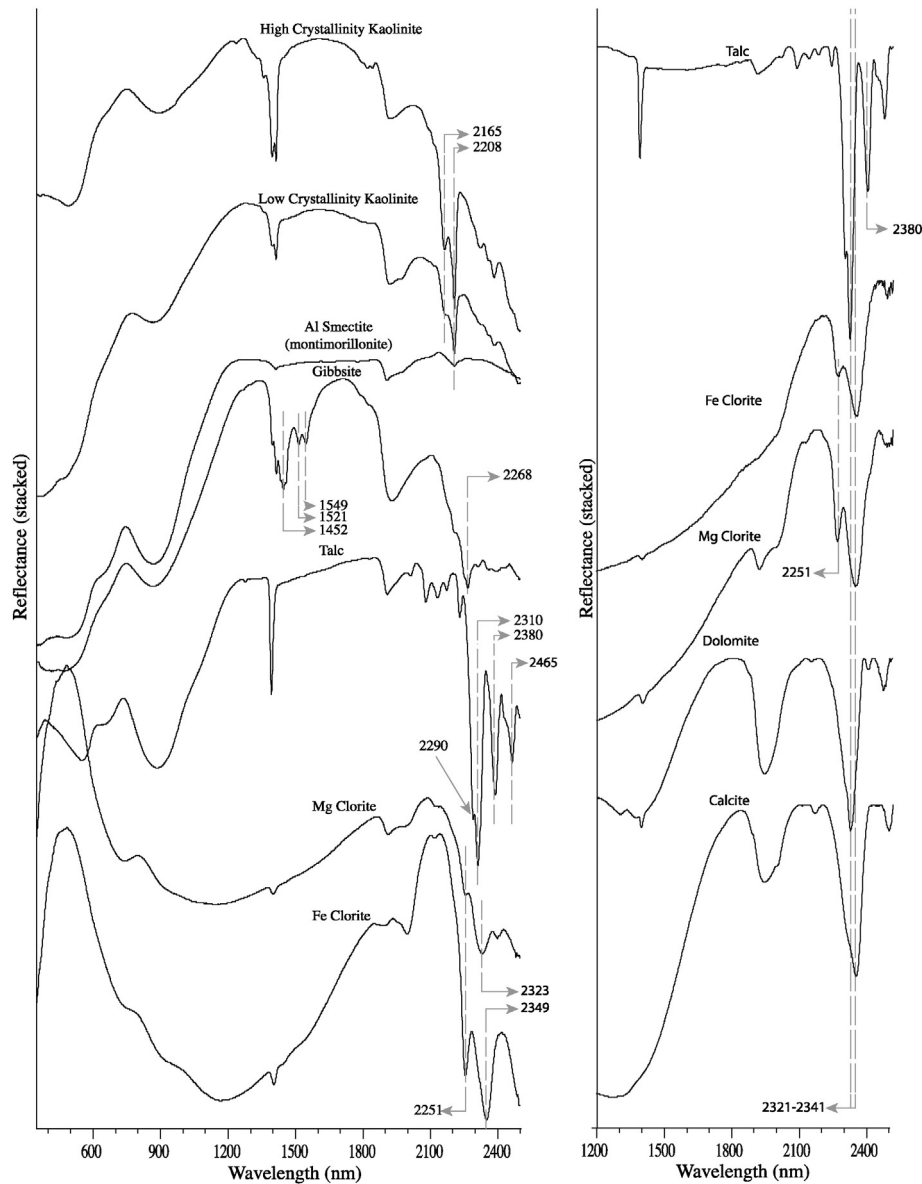
Fig. 6. Stacked reflectance spectra of the samples containing iron (hydro-)oxides, phyllosilicates and carbonate of the N4WS deposit, including kaolinite (F1495/014, F1012/130), Al smectite (F1115/025), gibbsite (F1515/22), talc (F1515/194), chlorite (F1115/092, F1398/144), dolomite (F1515/231) and calcite (F1398/090). All samples contain iron (hydro-)oxides. The main absorption features of these minerals are highlighted.

The aluminous smectites do not have the additional absorption features between 2160 and 2190 nm that occur in the kaolinite-group minerals (Fig. 6; Clark et al., 1990), and they typically contain structural water (deep and asymmetric sharp absorption at 1910 nm). Aluminous smectite and kaolinite-group minerals were distinguished using the following condition: 2160D2190 < 0.001 (Table 1). To obtain the abundance of aluminous smectite, the depth of the absorption feature at 2208 nm, which is also present in kaolinite, was calculated. The absorption feature was calculated using a tenth-degree polynomial fitted to the spectral curve removed from the continuum between 2150 and 2267 nm, with a focus between 2193 and 2225 nm (2200Ds, Tables 1 and 2). Also, the algorithm discarded mixtures with kaolinite and gibbsite.

Gibbsite has a strong characteristic absorption feature near 2268 nm and three less prominent absorption features at 1452, 1521 and 1549 nm in continuum removed spectra (Fig. 6; Clark et al., 1990). The abundance of gibbsite was obtained from the calculation of the depth of the absorption feature at 2268 nm using a twelfth-degree polynomial fitted to the continuum removed spectrum between 2115 and 2475 nm, with the focus between 2235 and 2300 nm (2260D, Tables 1 and 2). The gibbsite was identified using the following condition: 1450D > 0.011 and 2260D > 0.009. Also, the algorithm did not accept mixtures with kaolinite and Al-smectite.

The Mg—OH bonds present in talc produce a characteristic absorption feature near 2310 nm and 2380 nm and a minor absorption feature at 2290 nm in continuum removed spectra (Fig. 6; Clark et al., 1990). In addition to these features, talc has the hydroxyl absorption feature at 1400 nm, which is also present in the other phyllosilicates. The abundance of talc was obtained from the depth of the absorption feature at 2310 nm calculated using a twelfth-degree polynomial fitted to the continuum removed spectrum from 2242 to 2342 nm, with a focus ranging between 2305 and 2320 nm (2310D, Tables 1 and 2). To obtain this parameter, the algorithm used the depth of the features at 2380 and 1400 nm (2380D, 1400D, Table 1) to distinguish talc from carbonates and chlorite (Fig. 6).

These minerals also absorb near 2310 nm. Also, the algorithm did not accept mixtures with chlorite and carbonate. Thus, the conditions were 2380D > 1, 1400D > 0.0039, carbonate and chlorite abundance = 0.

Chlorite has two characteristic absorption features, with one from 2240 to 2256 nm and the other from 2320 to 2360 nm in continuum removed spectra, related to Fe—OH and Mg—OH bonds, respectively (Hunt and Salisbury, 1970). The absorption associated with Fe—OH bonds (near ~2251 nm) distinguishes chlorite from talc and carbonates. These minerals also contain Mg—OH and/or CO_3 absorbing at wavelengths near the main absorption feature of chlorite located from 2320 to 2350 nm in continuum removed spectra (Fig. 6; Gaffey, 1986a; Clark et al., 1990). The position of this absorption feature varies with the composition, ranging from 2320 nm for magnesian chlorites to 2350 nm for ferrous chlorites in continuum removed spectra (Hunt and Salisbury, 1970). The abundance of chlorite was obtained by calculating the depth using a twelfth-degree polynomial fitted to the continuum removed spectrum from 2171 to 2439 nm, with a focus ranging between 2300 and 2379 nm (2335D, Tables 1 and 2). The composition of the chlorite was calculated using a twelfth-degree polynomial fitted to the continuum removed spectrum from 2272 to 2381 nm, with a focus ranging between 2310 and 2370 nm (2335Wvl, Table 1 and Table 2). The algorithm used to obtain these parameters employed the depth of the absorption feature at 2251 nm (2250D, Table 1) to distinguish chlorite from talc and carbonates. Additionally, the algorithm discarded mixtures with talc, carbonate and gibbsite because this mineral has similar absorption features to chlorite. Thus, the conditions necessary to execute the algorithm were 2250D > 1 and abundance of talc, carbonate and gibbsite = 0.

The vibrations of CO_3^{2-} ions produce strong absorption features from 2500 to 2550 nm and 2300–2350 nm and minor absorption features from 2120 to 2160 nm, 1970–2000 nm and 1850–1870 nm in continuum removed spectra (Fig. 6; Gaffey, 1986b; Clark et al., 1990). The position of these features varies with the composition, ranging from ~2315 nm for dolomite to ~2350 nm for calcite (Gaffey, 1986a). The abundance of carbonates in the samples was assessed from the depth of a tenth-degree polynomial fitted to the continuum removed spectrum from 2250 to 2360 nm, with a focus ranging between 2310 and 2345 nm (2330D, Tables 1 and 2). The composition of carbonates was calculated from a tenth-degree polynomial fitted to the continuum removed spectrum from 2250 to 2360 nm, with a focus ranging between 2310 and 2345 nm (2330Wvl, Tables 1 and 2). Both the abundance and composition of carbonates were calculated only for samples that had no chlorite and/or talc. These minerals also absorb from 2300 to 2350 nm, the same region of the main absorption feature of carbonates used for calculations; however, they also have other diagnostic absorption features (Clark et al., 1990; Post and Noble, 1993; Bishop et al., 2008). Chlorite, for example, has a diagnostic absorption feature at ~2255 nm, which is identified by the parameter 2250D (Table 1). Talc has an extra absorption feature at ~2380 nm, which is identified by the parameter 2380D (Table 1). Therefore, the conditions to calculate the spectral parameters of the carbonates were 2380D < 1, 2250D < 1.004, talc and chlorite abundance = 0. In addition to these conditions, the strong asymmetry and the minimum depth of the 2330 nm feature were also considered (2330Asym > 1.11 and 2330D > 1.003, Table 2).

2.3. Validation and analysis of spectral data

2.3.1. Abundance of iron (hydro-)oxides

The iron (hydro-)oxide abundance algorithm (900D, Table 1) was compared to the %Fe_2O_3 from the XRF analyses of the drill cores. The depth of the absorption feature at ~900 nm (900D, Table 1) is significantly correlated with the XRF data despite the large observed scattering. A first-order polynomial was used for the correlation, which had a root-mean-square error (RMSE) of 11.6% Fe_2O_3. (Fig. 7; 2007 samples). The samples were filtered for the correlation, and only pure hematite spectra were selected for the correlation. Samples of hematite mixed with other Fe-bearing mineral, like chlorite, were discarded. Samples of minerals that have no iron, like kaolinite, also influence the 900D parameter and were also discarded. To better understand what is

causing this influence, the albedo (N1650R) of these samples were compared to the 900D feature and the % Fe_2O_3 from the XRF analyses (Fig. 8A and B). Fig. 8A shows that impure spectra, especially those mixed with kaolinite, have higher albedo than pure spectra. Although most of them have low % Fe_2O_3, the 900D parameter of these samples are in the same range of samples with higher % Fe_2O_3. However, the depth of the 900 nm absorption feature should be proportional to the % Fe_2O_3. Haest and Cudahy (2012) observed that the depth of the ~900 nm absorption feature is correlated to the albedo, so abundance values were underestimated in darker samples and overestimated in lighter samples. This can be explained by a combination of grain size variations and the effect of opaque minerals, reducing the length of the actual path taken by electromagnetic energy, decreasing the interaction/absorption of specific minerals (Clark and Roush, 1984). Consequently, samples mixed with bright minerals, like kaolinite, gibbsite, Al-smectite and carbonate will have their 900D overestimated and will not show a good correlation to Fe_2O_3 from XRF.

The low correlation obtained in this study may be because of unidentified spectral mixing and/or lack of pure spectra. Also, the spectra were obtained directly from half cut samples of drill core, while XRF data were obtained for pulverized samples of the corresponding other half. Therefore the sample used for infrared analysis might not be fully representative of the sample used for XRF, which will increase the RMSE when correlating XRF results against element predictions from infrared mineralogy.

To understand the spectral behaviour of the different analysed rocks, the samples in Fig. 7 were plotted according to the type of rock (jaspilite, hematite, basalt, etc.). The colour for each lithotype matches the same pattern used in the geological description in several studies performed in Carajás to facilitate data integration. The graph shows that the different lithotypes were grouped into two domains. Jaspilite has an intermediate Fe_2O_3 percentage (40 to 65%) and exhibited 900D parameter values ranging from 0.05 to 0.38. Friable hematite represents the main ore in the deposit, with high Fe_2O_3 percentage (>90%) and exhibited
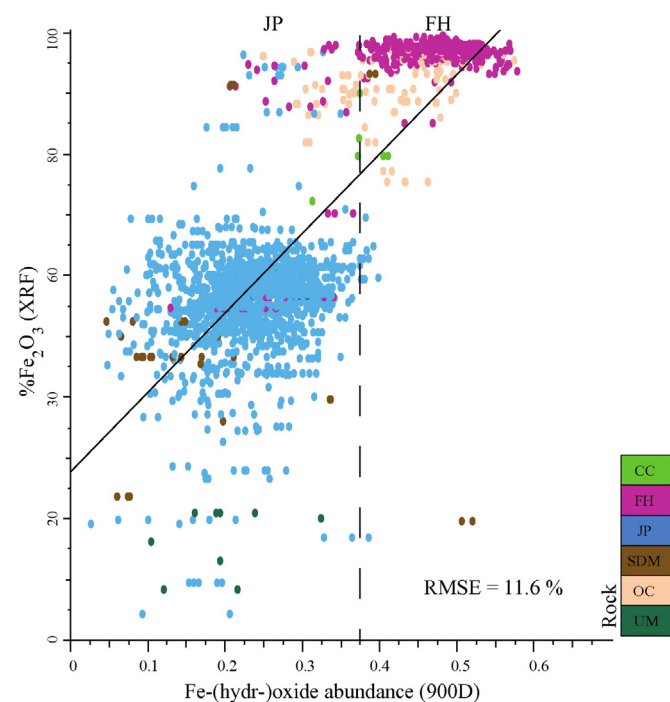

Fig. 7. Correlation between the iron (hydro-)oxide (900D) abundance algorithm and % Fe_2O_3 of the XRF analyses for spectra with only iron (hydro-)oxide; the regression curve is shown. Number of samples: 2007. The samples are coloured according to the type of rock. CC: chemical canga; FH: friable hematite; JP: jaspilite; SDM: semi-decomposed mafic; OC: ore canga; UM: mafic rock. (For interpretation of the references to colour in this figure legend, the reader is referred to the web version of this article.)
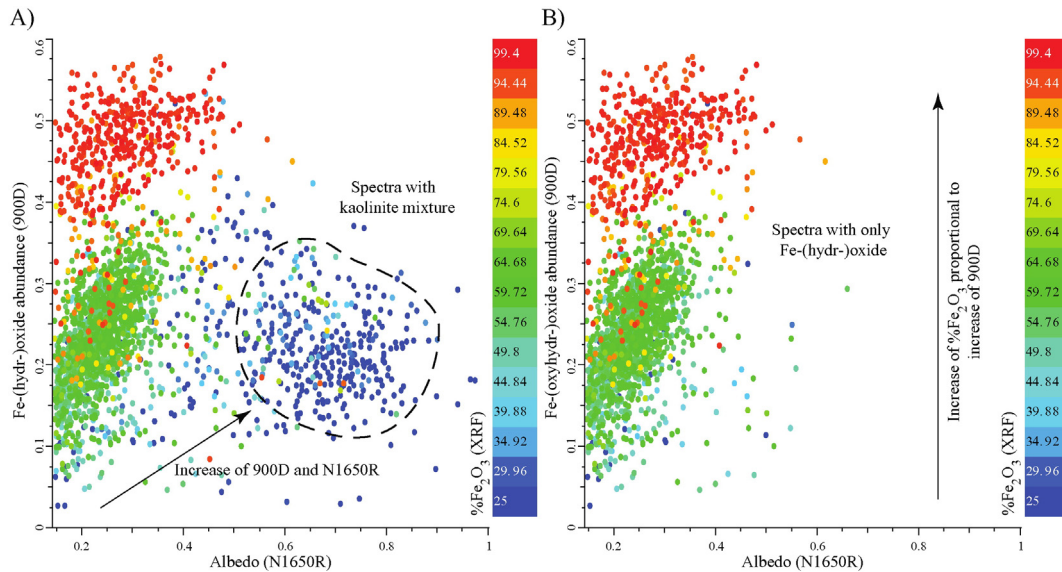
Fig. 8. A) Correlation between the albedo (N1650R) and iron (hydro-)oxide (900D) abundance algorithm for spectra with iron (hydro-)oxide, including spectra with kaolinite mixture. Number of samples: 2501. B) Correlation between the albedo (N1650R) and iron (hydro-)oxide (900D) abundance algorithm for spectra with only iron (hydro-)oxide. Number of samples: 2007. In A) and B), the samples are coloured according to the %Fe_2O_3 of the XRF analyses. (For interpretation of the references to color in this figure legend, the reader is referred to the web version of this article.)

900D parameter values >0.38. Thus, in addition to providing an estimate of the Fe_2O_3 content in the sample, the spectral analysis can differentiate ore from other rocks of the deposit.

2.3.2. Composition of the iron (hydro-)oxides (hematite-goethite)

The accuracy of the algorithm that determines the hematite-goethite distribution (Table 2) was validated using the loss on ignition (LOI) data of the samples (goethite dehydrates to hematite in the 260 to 425 °C temperature range; Strezov et al., 2010).

Because the LOI measured for heating to 1000 °C is affected by a number of minerals (goethite, Al—OH clays and organic and inorganic carbon (carbonates)), only the samples with low Al_2O_3, CaO and MgO content and high Fe_2O_3 (CaO < 1%, MgO < 1%, Al_2O_3 < 2.5% and Fe_2O_3 > 55%) content were used to validate the goethite-hematite distribution algorithm. These samples showed low correlation between the values of the algorithm and LOI results, with clustering near the hematite wavelengths (Fig. 9; 1285 samples). The goethite samples showed high LOI values (~8%) and absorption wavelengths longer than 890 nm, whereas the samples richest in hematite showed low LOI values (~2%) and absorption wavelengths shorter than <890 nm. Fig. 9 clearly shows the predominance of hematite in the N4WS deposit, explaining the low correlation.

2.3.3. Abundance of aluminous clays

The accuracy of the 2200DK and 2260D algorithms (Table 1) in measuring the amount of kaolinite and gibbsite, respectively, was evaluated using the percentage of Al_2O_3 of the XRF analyses of drill cores.

The 2200DK spectral parameter showed moderate linear correlation compared with the percentage of Al_2O_3 and had an RMSE value of 6.0% Al_2O_3 (Fig. 10A; 788 samples). These samples with identified kaolinite were plot in a SiO_2 versus Al_2O_3 graph (Fig. 10B). Most of them (~75%) plot along the line towards pure kaolinite composition (46.6% SiO_2 and 39.5% Al_2O_3), showing the absence of others Al- and Si-bearing minerals on most correlated samples. Some samples (~20%) plot between the kaolinite line and the SiO_2 axis, showing SiO_2 enrichment, probably caused by quartz and/or chlorite mixture. About 5% of samples plot between the kaolinite line and the Al_2O_3 axis, showing aluminum enrichment, probably caused by gibbsite mixture. The 2200DK parameter was filtered with masks to avoid mixtures with gibbsite, Al-smectite and chlorite. Petrographic studies showed that some of

these minerals are still present in filtered kaolinite samples in such low amounts that they do not generate diagnostic absorption features in the spectra. The samples with unidentified spectral mixtures decrease the correlation between the kaolinite abundance and the %Al_2O_3.

The algorithm 2260D showed a low linear correlation with a higher RMSE of 10.4% Al_2O_3 (Fig. 10C). The samples with identified gibbsite were plot in a SiO_2 versus Al_2O_3 graph (Fig. 10D). About 98% of the samples plot along the zero SiO_2 line, showing absence of other Al-bearing minerals in these samples. The accuracy is within the error range of 5 to 10% reported by Zhang et al. (2001) in the quantification of clays using absorption features related to clays in the SWIR.

The Al-smectite abundance algorithm cannot be correlated with the percentage of Al_2O_3 measured in the XRF because of the small depth of the absorption feature at ~2200 nm (2200DS) in most of the analysed samples.

2.3.4. Abundance and composition of chlorite

The chlorite (2335D) abundance algorithm was correlated with the percentage of Fe_2O_3 + MgO obtained in the XRF analyses. Spectra with other Mg bearing minerals (talc, carbonate) are discarded by
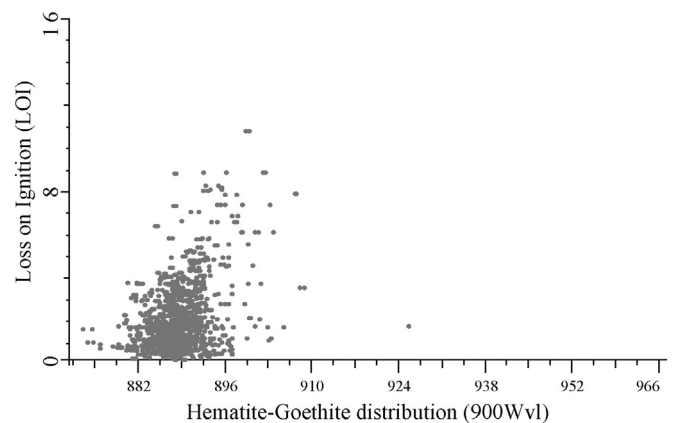

Fig. 9. Correlation between the distribution of goethite-hematite (900Wvl) and loss on ignition (LOI) at 1000 °C for samples with XRF analyses falling within the following limits: CaO < 1%, MgO < 1%, Al_2O_3 < 2.5% and Fe > 55%. Number of samples: 1285.
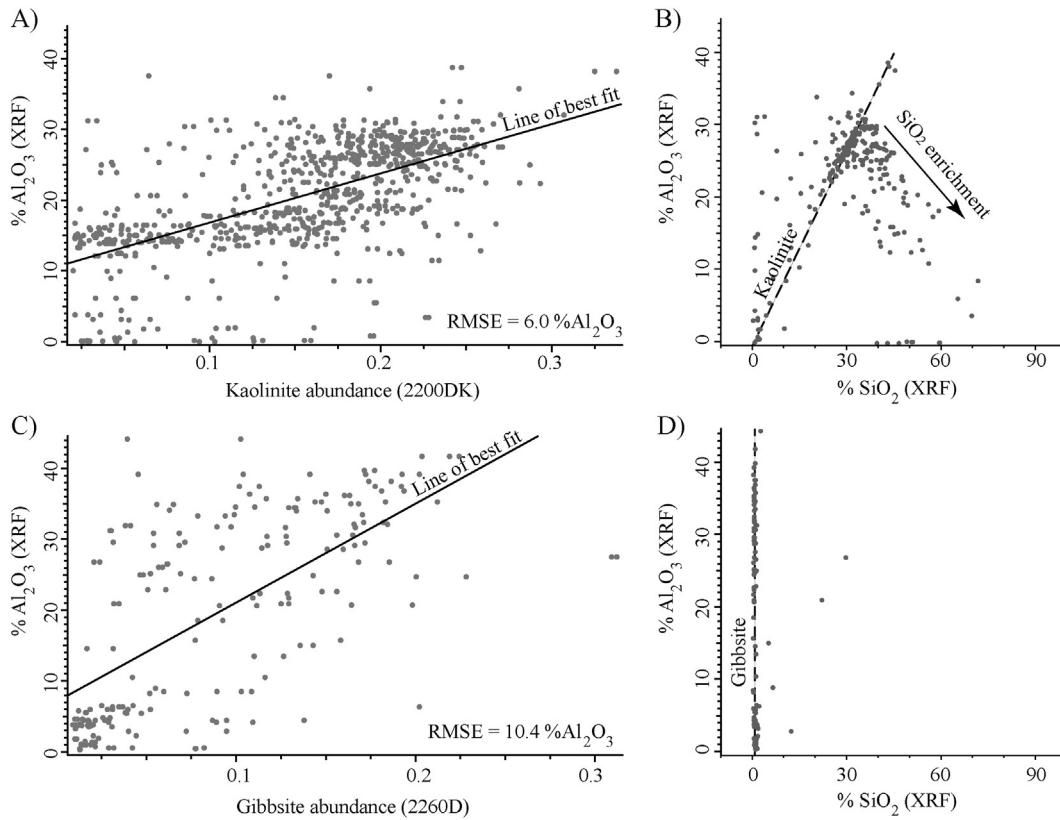
Fig. 10. A) Correlation between kaolinite (2200DK) abundance and %Al_2O_3 (XRF; 788 samples). B) SiO_2 vs. Al_2O_3 for samples with kaolinite abundance (2200DK) greater than zero. Dashed line from zero towards pure kaolinite expected composition (39.5% Al_2O_3 and 46.6% SiO_2). C) Correlation between gibbsite (2260D) abundance and %Al_2O_3 (XRF; 205 samples). Dashed line along zero SiO_2, showing pure gibbsite expected composition. D) SiO_2 vs. Al_2O_3 for samples with gibbsite abundance (2260D) greater than zero.

filtering. The abundance of chlorite (2335D) did not show a significant linear correlation with the percentage of Fe_2O_3 + MgO. However, all the identified chlorites are from the metamorphism of the mafic rocks of the N4WS deposit. Therefore, an increase in the abundance of chlorite is not necessarily related to the iron and magnesium enrichment of the mafic rocks.

The composition of chlorite, obtained by the parameter 2335Wvl, was correlated with the %MgO/%MgO + %Fe_2O_3 of the XRF analyses (Fig. 11). Samples with the longest wavelength of the 2335 nm absorption feature show a lower percentage of MgO and higher of Fe_2O_3 in the XRF analyses. Samples with the shortest wavelengths of the 2335 nm feature show a greater percentage of MgO in the analyses. The

histogram also shows that Mg-chlorites predominate in the N4WS deposit samples.

2.3.5. Abundance of talc

The absorption feature at ~2310 nm (2310D) used in the talc abundance algorithm was correlated with the %MgO obtained in the XRF analyses of the drill cores (Fig. 12; 242 samples). The 2310D algorithm showed a low correlation with the %MgO of the XRF analyses, which had an RMSE value of 7.9% MgO. Certain samples with high %MgO in the XRF analyses had a low depth of the absorption feature at ~2310 nm (2310D). The heterogeneous distribution of talc in the samples makes it difficult to obtain spectra representing the chemical
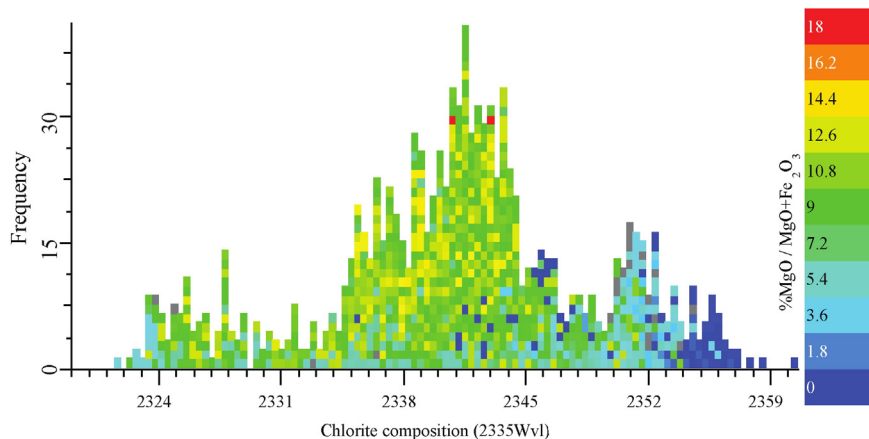

Fig. 11. Histogram of the chlorite composition obtained by the 2335Wvl algorithm. The histogram bars are coloured according to the %MgO/%MgO + %Fe_2O_3 obtained by the XRF analyses of the samples. (For interpretation of the references to colour in this figure legend, the reader is referred to the web version of this article.)

composition of the entire sample; thus, spectra were obtained from regions with distinct talc concentrations in the same sample, affecting the correlation.

2.3.6. Abundance and composition of carbonates

The carbonate abundance algorithm was validated using the sum of the percentage of CaO and MgO obtained in the XRF analyses. The depth of the absorption feature at ~2330 nm (2330D) in the carbonates showed a low correlation with the %CaO + %MgO, and it had an RMSE value of 6.8% CaO + MgO (Fig. 13A; 70 samples). However, the small number of samples with carbonates hinders the correlation of these data.

The carbonate composition algorithm was validated using the %CaO and %MgO data from the XRF analyses. The %CaO and %MgO of the samples with carbonate are shown in Fig. 13B and coloured according to the wavelength of the 2330 nm feature (Composition of carbonates, Table 2). The line in Fig. 13B (%CaO = 1.6 × %MgO) represents the line at which the dolomite samples with ideal composition (CaMg(CO$_3$)$_2$) should be located to comply with the stoichiometric ratios between the percentages of Ca and Mg because the molar mass of Ca is 1.6 times greater than that of Mg. Samples located along this line have an absorption feature related to CO$_3^{2-}$ (2330Wvl) between 2321 and 2330 nm (blue to green, Fig. 13B), indicating dolomitic carbonates with more MgO (Gaffey, 1986a; Clark et al., 1990), which is consistent with the geochemical data obtained with XRF. Samples above the dolomite line have a 2330 nm feature at higher wavelengths ranging between 2330 and 2343 nm, indicating calcitic carbonates poor in magnesium, (Gaffey, 1986a; Clark et al., 1990), which is consistent with the %CaO increase determined by the XRF analyses.

2.4. Spatial analysis of the spectral parameters

2.4.1. Spectral characterisation of the lithotypes mapped in N4WS

The spectral parameters obtained by the algorithms in Table 2 were used for the in-depth spatial analysis of the nine drill cores. The mineral abundance, crystallinity and composition data obtained from the spectra, geochemical analyses (XRF) and the magnetic susceptibility were used to characterize the lithotypes described and determine areas with similar chemical composition and mineralogy. The spectral characteristics observed are described below.

OC: abundance of iron (hydro-)oxides (900D) in OC varies between 0.1 and 0.3 and is similar to the variation observed in jaspilites. However, the presence of gibbsite, identified by the 2260D algorithm allows its differentiation from JP and FH. The geochemical data show that this lithotype has higher %Al$_2$O$_3$ (XRF) than JP, which is consistent with
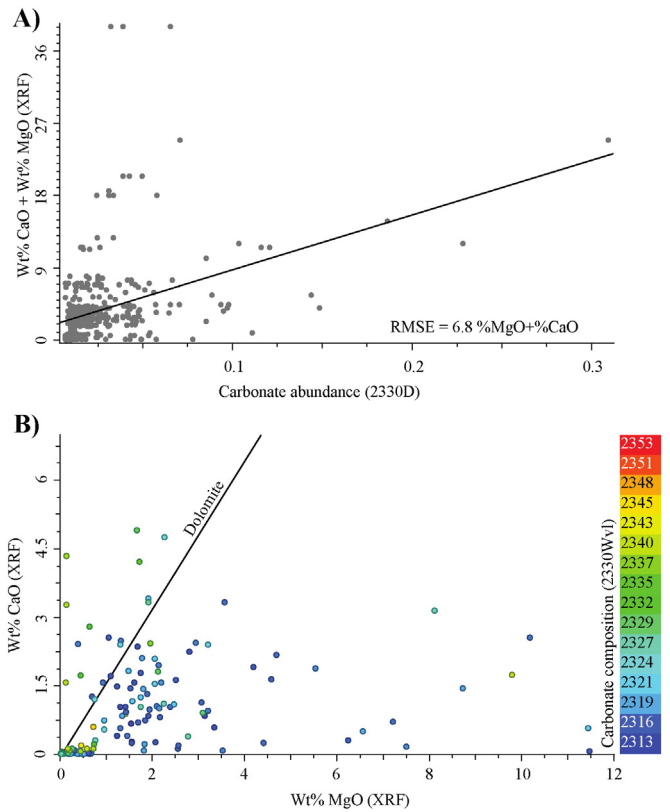
Fig. 13. A) Correlation between carbonate (2330D) abundance and %CaO + %MgO of the XRF analyses. The line shows the linear function that best fits the data. Number of samples: 70. B) %CaO vs. %MgO measured by XRF for the samples with carbonate identified through the reflectance spectrum by the 2330D algorithm. The samples are coloured according to the wavelength of the absorption feature at 2330 nm, which was obtained by the 2330Wvl algorithm. Number of samples: 70. (For interpretation of the references to colour in this figure legend, the reader is referred to the online version of this chapter.)

the identification of gibbsite in the spectra (Fig. 15, interval of 45–65 m and Fig. 16, interval of 0–20 m);

CC: similar to the OC, CC has an iron (hydro-)oxide (900D) abundance similar to the JP. The abundance of gibbsite, identified by the 2260D algorithm, is greater than that of OC as well as the %Al$_2$O$_3$ (XRF). Certain spectra obtained for the regolith of the mafic rock indicate the presence of talc (Fig. 15, interval of 0–45 m);

JP: The spectral parameters differentiated JP in four domains, namely: hematite-rich JP (JP(H)), hematite-goethite-rich JP (JP(HG)), JP with talc (JP(T)) and JP with carbonate (JP(C)). The abundance of iron (hydro-)oxides (900D) is similar in the four domains and varies proportionally to the total %Fe$_2$O$_3$ (XRF; Figs. 15 and 16).

The HG distribution obtained by the 900Wvl algorithm (Table 2) was able to differentiate JP(H) and JP(HG). The JP(H) showed 900Wvl values ranging between 872 and 890 nm, which were lower than the values found in JP(HG) (Fig. 15, interval of 140–330 m and Fig. 16, interval of 215–255 m). The increased 900Wvl in JP was related to an increased supergene alteration because JP near the surface has the higher values of 900Wvl (Fig. 15) as well as to the proximity of brecciated zones (interval between 360 and 530 m Fig. 15). Goethite and magnetite, most likely of hydrothermal origin, were found near breccias, such as those described in the study of Lobato et al. (2005b). These changes on the 900Wvl position can be due hematite goethite mixtures, however, the 900Wvl-LOI crossplot shows no samples with 900Wvl towards 950 and LOI towards 8–10, so there are probably no goethite rich samples present at this deposit in Carajas. Therefore, the changes on the 900Wvl position also can be due the grain size, grain shape, orientation, packing density, matrix composition (Adams and Filice, 1967;
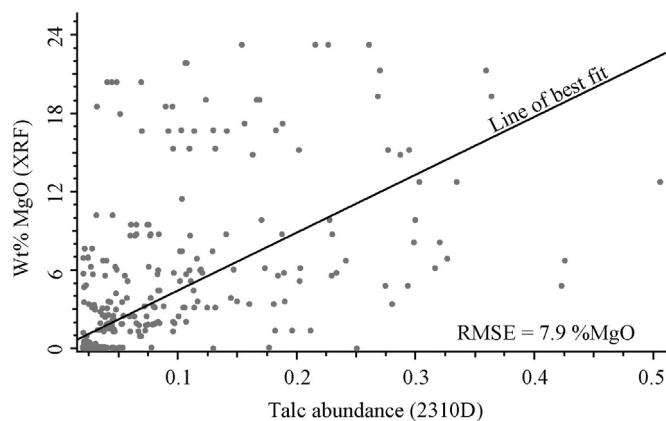

Fig. 12. Correlation between the abundance of talc obtained by spectral analysis of the samples (algorithm 2310D) and %MgO obtained by XRF analysis. The line shows the linear function that best fits the data. Number of samples: 242.

Sherman, 1985; Sherman et al., 1982; Morris et al., 1985; Singer and Roush, 1985) and mixtures with other minerals that have absorption features near to 900Wvl position, like magnetite.

The JP(C) domain can be differentiated from other domains by the carbonate abundance algorithm 2330D (Table 2; Fig. 15, intervals of 390–400 m and 475–530 m, and Fig. 16, interval of 280–310 m). The samples from this domain had a 2330D index that is superior to all other lithotypes as well as the %CaO (XRF) and %MgO (XRF). In the JP(C) domain, the identification of talc was also possible in certain samples through the 2310D algorithm. The magnetic susceptibility in this domain was higher than in the others, reaching 0.75 (SI unit). Some samples of the JP(C) domain were analysed under a microscope, which confirmed the presence of carbonate and talc. These minerals fill the veinlets of brecciated jaspilite and disseminated in the jasper bands, replacing the primary mineralogy consisting of quartz and hematite. In addition, most of the samples from this domain have porphyrotopes of magnetite in transition to hematite (Fig. 14F).

The samples from JP(C) zones have a large number of veins filled by carbonates and several brecciated regions (Fig. 14A). Although the entire interval has been described as JP in the recording of the core, these brecciated regions had already been detected during previous recording. However, the areas abundant in talc, which surround the carbonate areas, had not been detected during recording of the core because of the difficulty of visually identifying talc in JPs. The same relationship was observed in other drill cores, where the intervals of JP(C) are surrounded by intervals of JP(T). The appearance of talc in JP(T) intervals may be related to a distal hydrothermal alteration of JPs promoted by the fluids involved in the carbonate veining/brecciating of the JP(C) domain. These brecciated JP intervals can be correlated with the hydrothermalised areas described in Lobato et al. (2005b, 2008); Rosière et al. (2006) and Figueiredo e Silva et al. (2008); Figueiredo e Silva et al., 2011).

FH: The abundance of iron (hydro-)oxides found by the 900D algorithm in the FH is greater than the abundance found in the OC and in the JP, with the 900D index ranging from 0.25 to 0.5. The FH has a large variation in the 900D index, however the %Fe$_2$O$_3$ varies little. Therefore, this variation on the 900D index is not due a variation on the hematite abundance of the samples but probably due changes on grain size, grain shape, orientation, packing density and matrix composition of these samples (Adams and Filice, 1967; Sherman et al., 1982; Morris et al., 1985; Sherman, 1985; Singer and Roush, 1985). Similar to the JPs, the distribution of hematite-goethite (900Wvl) can be used to distinguish FH in hematite (H) and hematite-goethite (HG). The FH has 900Wvl index values ranging between 872 and 890 nm, lower than the values found in FH with the highest 900Wvl index (HG; Fig. 16, interval of 20–190 m).

UM and SDM: Fresh or semi-altered mafic rocks are characterised by the presence of chlorite and/or kaolinite and identified by the 2335D and 2200 K algorithms, respectively. These spectral parameters allowed their differentiation in two domains, namely: mafic rock with chlorite predominance (M(Cl)) and mafic rock with kaolinite predominance (M(K)). The intervals more abundant in chlorite (M(Cl)) are correlated with UM (Fig. 15, interval of 535–560 m, and Fig. 16, interval of 330–350 m). An analysis of the sections of this unit showed that chlorite is the most abundant alteration mineral in the mafic rocks (Fig. 14H and I). According to Zucchetti (2007), a portion of the chlorite crystals was formed by submarine hydrothermal alteration and recrystallised during regional metamorphism. Subsequently, a new generation of chlorite formed during the hydrothermal alteration to chlorite + hematite. The composition of chlorite identified by the 2335Wvl algorithm in these domains can be used to distinguish intervals where Fe-chlorites are predominant from intervals where Mg-chlorites are predominant. The variation in chlorite composition may be the result of supergene alterations of mafic rocks; however, Zucchetti (2007) proposed that there is a compositional variation in hydrothermal chlorites, with the Mg-chlorites associated with oxidising hydrothermal fluids that promote

the crystallisation of hydrothermal hematite together with chlorite. The M(K) domain is correlated with SDM (Fig. 15, interval of 100–140 m) because the appearance of kaolinite indicates a greater degree of supergene alteration of the mafic rocks. The kaolinite crystallinity, obtained by the parameter 2170SL, can be used to distinguish intervals in the M(K) domain with a predominance of low crystallinity kaolinites, associated with fault zones or fractures.

2.4.2. Correlation of spectral parameters in 2D

After performing a spectral characterisation of the lithotypes described in drill cores, a two dimensional (2D) analysis was performed in which the spectral domains were correlated along the profile. Fig. 17 shows one of the interpreted profiles. To facilitate the correlation, boreholes that were not analysed in this study were added to the profile (analysed boreholes are highlighted in Fig. 17).

The spectral domains showed good correlations in the profile and helped to identify areas that were not distinguished in previous lithological correlations. The ease of identifying intervals of brecciated JP (JP(C)) and JP(T), facilitated determining the spatial distribution of these intervals in the profile. These intervals predominated at the base of the analysed cores, indicating that the brecciation related to carbonation/talcification of JPs occurred near the basal basalt of the cores. The JP(T) surround the brecciated JP(C), illustrating the relationship between talcification with brecciation and carbonation of JPs.

The hydrothermal hypogene model for the iron mineralisation of the Carajás Mineral Province proposed in Lobato et al. (2005b, 2008); Rosière et al. (2006) and Figueiredo e Silva et al. (2008); Rosiére et al., 2005) suggests that JPs richer in iron are found in brecciated zones that experienced leaching of silica and crystallisation of magnetite, hematite, goethite, chlorite, talc and sulphides. However, the brecciated JP found in the JP(C) and JP(T) zones had an abundance of iron (hydro-)oxide determined by spectral analysis (900D/1650R algorithm) and %Fe$_2$O$_3$ obtained by geochemical analysis similar to non-brecciated JPs. The JPs from the N4WS deposit, which is richer in iron, were strongly weathered, and represented by FH.

The correlation of spectral domains was also used to detail the contact between the OC and FH. The presence of clay minerals and increased abundance of goethite are characteristics of the OC that can be accurately identified by analysing the spectra, which can be used to differentiate OC from FH. Detailing the contact between these units is important for mine planning, because the identification and quantification of clay minerals, such as gibbsite and kaolinite, affect ore processing.

3. Conclusion

This study showed that reflectance spectroradiometry in the VNIR-SWIR regions can be used to characterize and evaluate the mineral distribution of an iron deposit. The main minerals found in the N4WS iron deposit were identified, including the ore mineralogy. Petrographical studies validate all the minerals identified by reflectance spectroradiometry. The algorithms developed to estimate the abundance and composition of minerals from the spectra data were validated using independent geochemical and LOI data. The error of spectral mineral abundance parameters, based on the correlation between elemental composition derived from infrared mineral estimates and XRF determined element concentrations, ranges between 6 and 11.6%. It cannot replace the geochemical analysis, but it can be useful as a quick estimation of the iron content and certain minerals associated with the deposit. The iron content obtained by these spectral parameters can be used for an expedited analysis of iron concentration and contaminant abundance of the ore. Hillier (2000) showed that quantitative analyses using the XRD results of clays and other minerals in sandstones and other rock samples in general are capable of producing results with ±3% accuracy and a confidence level of 95%. These routine analyses with XRD, however, require significant time for sample preparation
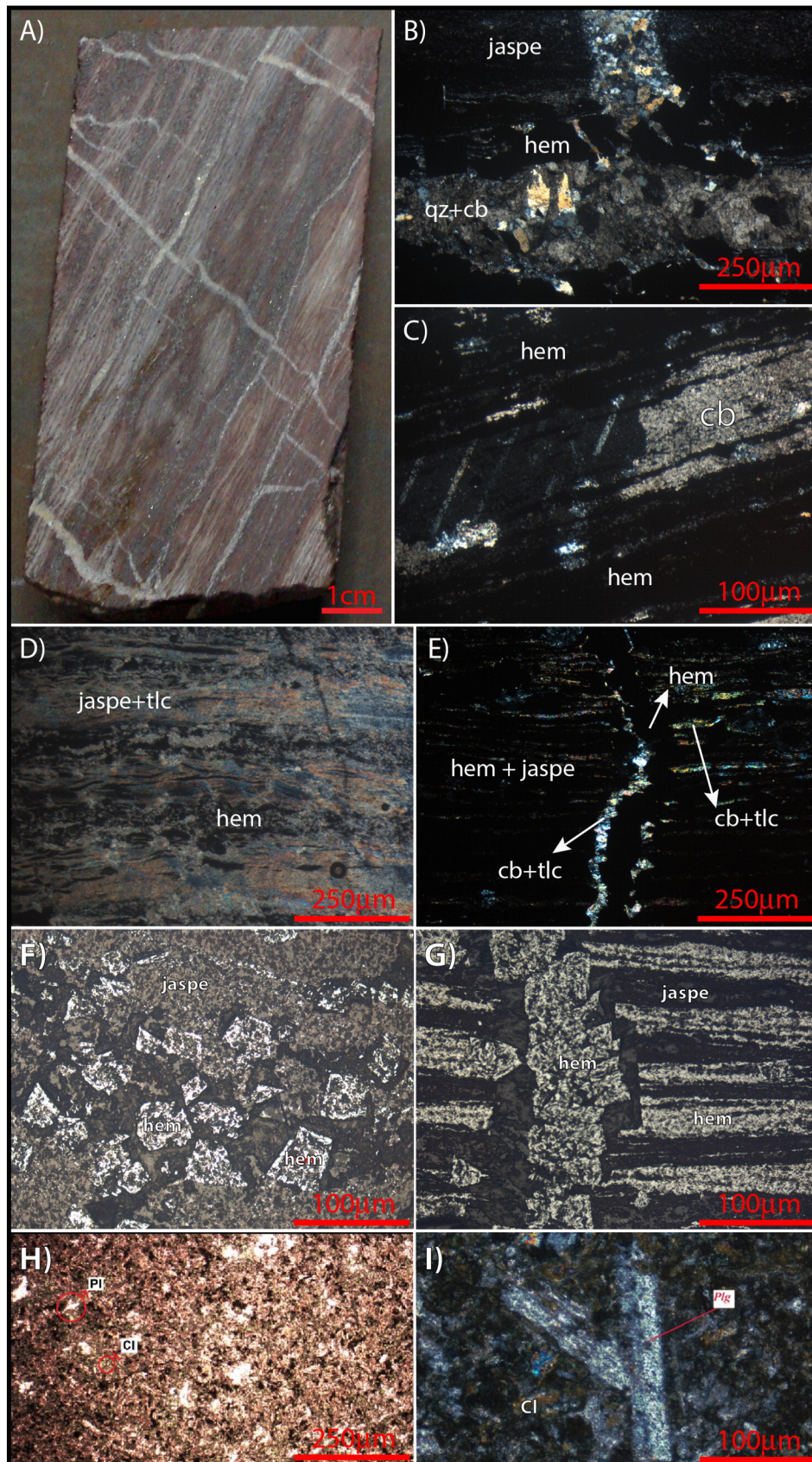
Fig. 14. A) Photo of brecciated jaspilite with carbonate veinlets (JP(C)). B) Photo of the brecciated jaspilite section (JP(C)) in transmitted light; in detail, veinlets filled with carbonate and quartz; crossed nicols. C) Photo of jaspilite with jasper bands replaced by carbonate in the transmitted light; crossed nicols. D) Photo of jaspilite with talc in the jasper bands section in transmitted light; crossed nicols. E) Jaspilite with veinlets filled with talc and carbonate. F) Photo of jaspilite with pseudomorphs of magnetite in reflected light. G) Photo of the section in reflected light of the photo detail in D), showing a veinlet filled by hematite. H) Photo of the fresh mafic (UM) section in transmitted light showing the preserved igneous texture; parallel nicols. I) Photo detail of H) with crossed nicols. Highlighted is a plagioclase crystal and matrix being altered to chlorite. hem, hematite; tlc, talc; cb, carbonate; qz, quartz; pl, plagioclase; and cl, chlorite.
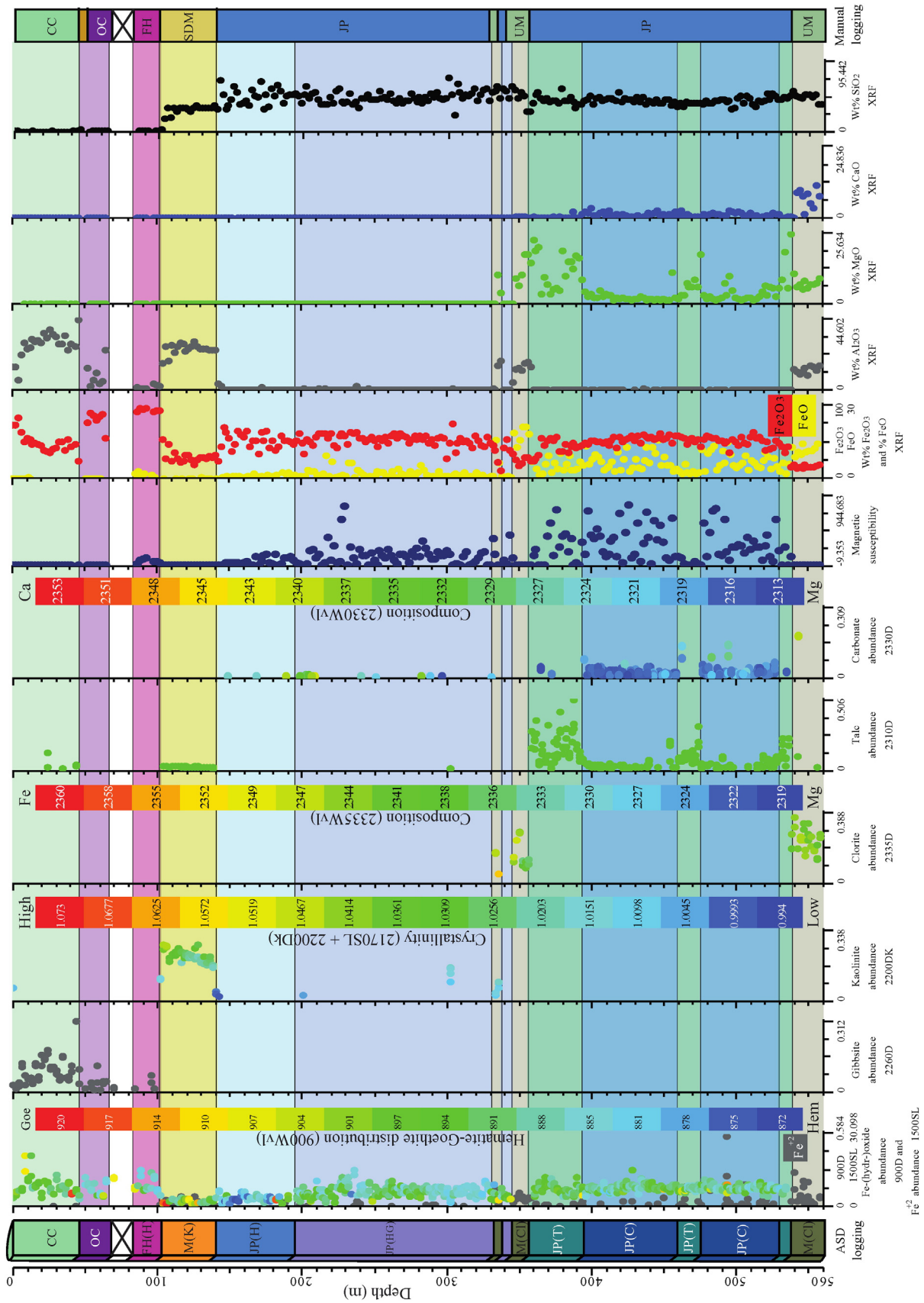
Fig. 15. Results of mineral abundance and composition analyses using the reflectance spectroscopy data for the F1515 drill core. The geochemical analysis of certain elements obtained by XRF, magnetic susceptibility and lithotypes described during the recording of the cores are also shown. The scatter plots show variations in mineral abundance as a function of depth. Certain diagrams are coloured in accordance with the changes in the composition of these minerals. The colour bars in the diagrams of abundance of iron (hydro-)oxides, chlorite and carbonate show the wavelength in nm of the absorption feature of these minerals. The diagram of abundance of kaolinite is coloured according to the crystallinity of kaolinite. The intervals that have similar mineralogical characteristics were grouped into the same colour horizons. (For interpretation of the references to colour in this figure legend, the reader is referred to the web version of this article.)
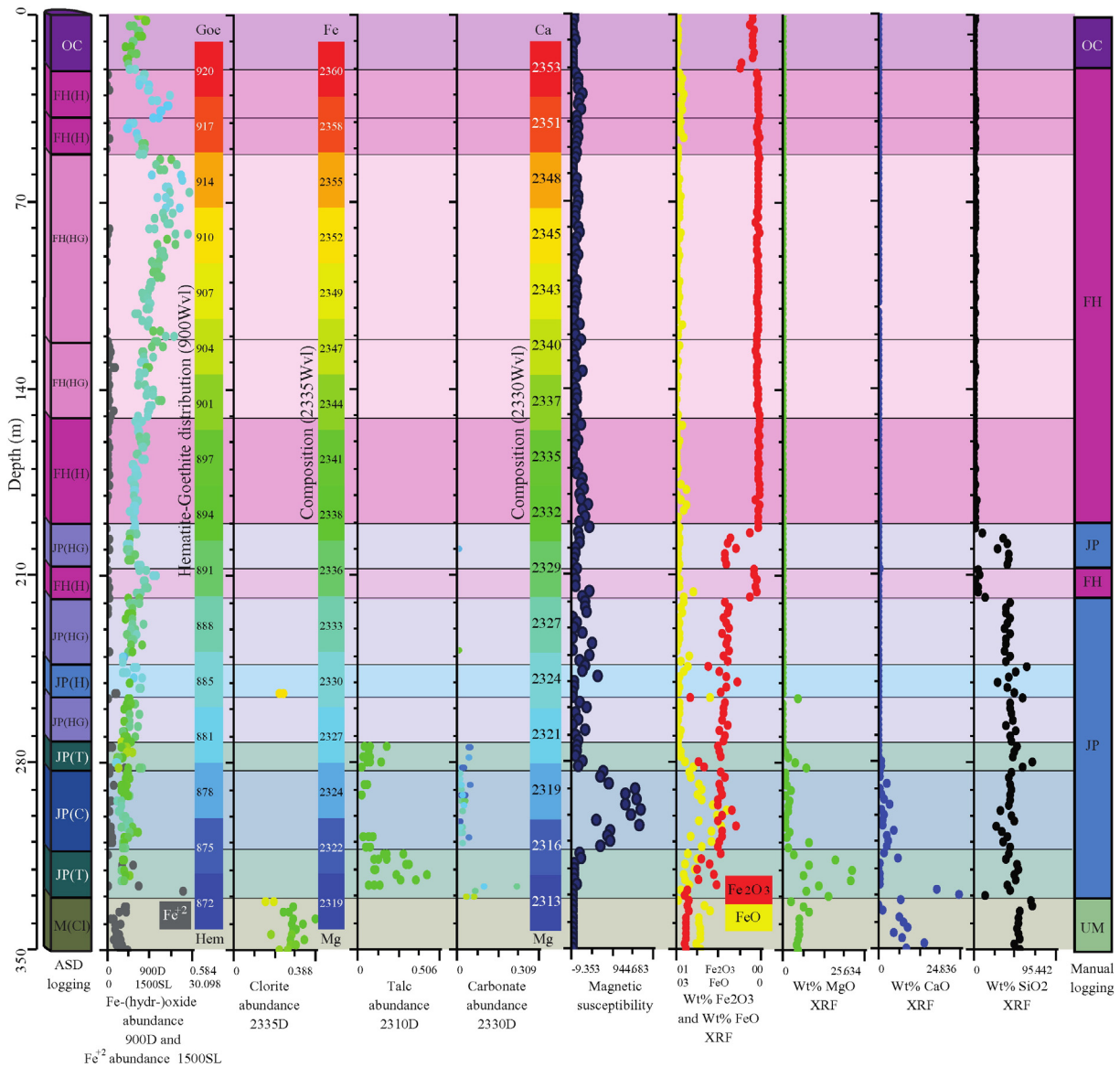
Fig. 16. Results of abundance and mineral composition analyses using the reflectance spectroscopy data for the F1051 drill core. The geochemical analysis of certain elements obtained by XRF, magnetic susceptibility and lithotypes described during the recording of the core are also shown. The scatter plots show variations in mineral abundance as a function of depth. Certain diagrams are coloured in accordance with the changes in the composition of these minerals. The colour bars in the diagrams of abundance of iron (hydro-)oxides, chlorite and carbonate show the wavelength in nm of the absorption feature of these minerals. The intervals that have similar mineralogical characteristics were grouped into the same colour horizons. (For interpretation of the references to colour in this figure legend, the reader is referred to the web version of this article.)

and data collection, and problems may still arise (e.g., preferential orientation, different smectite mixtures, etc.).

This study also shows that there are several limiting factors for the application of quantitative spectral parameters, as mineral complexity, heterogeneous mineral distribution on samples, mineral mixtures, mineral abundance below the detection limit of the technique, and others related to macro and micro physical properties of materials.

The analysis of the spectral parameters were capable of identifying the ore, protore and host rocks of the N4WS iron deposit described during the core recording, besides other new observations derived exclusively from the spectral data. Some of these observations are described below:

1. Minerals that had not been described before were identified in these rock types, such as the talc identified in some JP samples;
2. Zones with different physical properties that are difficult to differentiate on core logging were distinguished; e.g., zones with hematite were differentiated using the 900Wvl algorithm (hematite-goethite

distribution), where zones with similar position of the ~900 nm absorption feature were individualized. Although the majority of samples (>90%) have 900Wvl position of hematite, the position shifts some nanometers on certain core intervals.

3. Zones with higher oxide content were differentiated in the JP and FH intervals;
4. Zones with carbonate were differentiated in the JP intervals;
5. Chlorite composition was identified in the basalt intervals;
6. Basalts and semi-decomposed mafic were differentiated by the kaolin content obtained using the kaolinite abundance algorithm.

This study shows that quantitative spectral analysis is a very useful method of summarizing and presenting relevant mineral information from a large spectral data set obtained in drill cores. Therefore, quick spectral analyses of drill cores are of great value because they can easily generate information required by geoscientists for the mineralogical characterisation of geological environments. In addition, the universal applicability of these spectral algorithms is becoming realized because
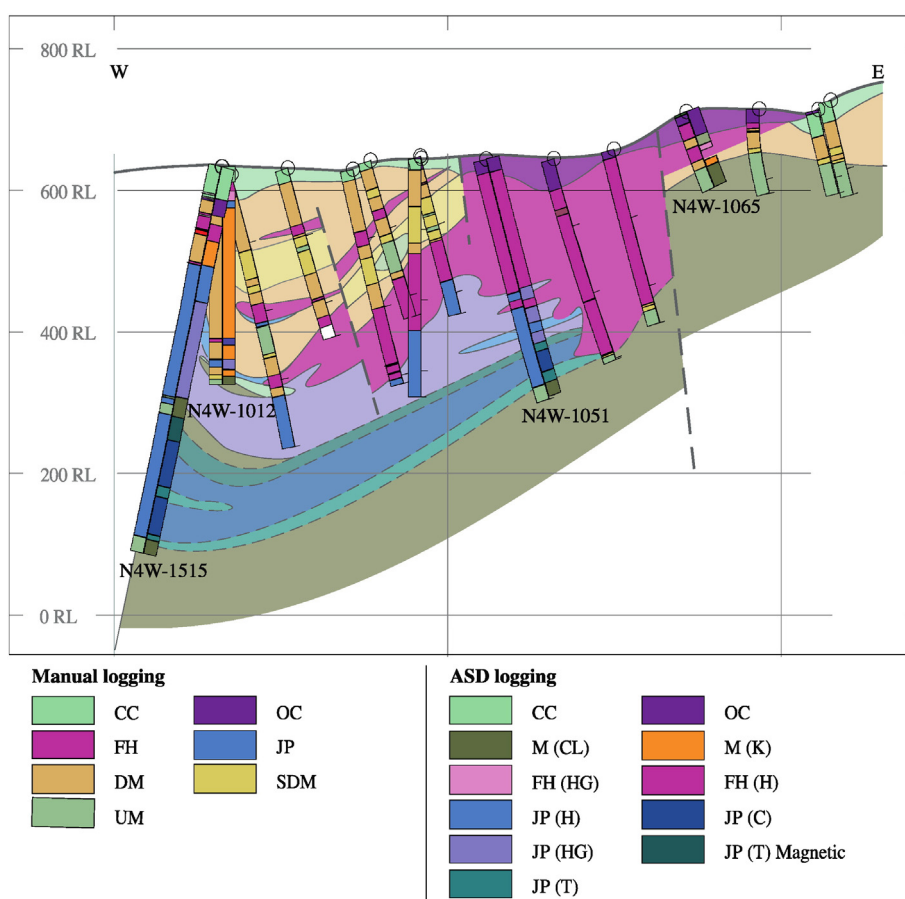
Fig. 17. Lithological section interpreted from the N4WS deposit running through the N4W-1515, N4W-1012, N4W-1051 and N4W-1065 cores (Fig. 2). The lithotypes were correlated according to the spectral domains, which represent compositional variations of the mapped lithologies. The unidentified cores were added to facilitate interpretation, and they only show the lithology. The dotted lines indicate possible faults. CC: chemical canga; OC: ore canga; FH: friable hematite; FH(HG): friable hematite with greater abundance of goethite; FH (H): friable hematite with lower abundance of goethite; JP: jaspilite; JP(H): hematite-rich jaspilite; JP(HG): jaspilite with goethite; JP(C): jaspilite with carbonate; JP(T): jaspilite with talc; DM: decomposed mafic; SDM: semi-decomposed mafic; UM: unweathered mafic; M(CL): mafic with chlorite; M(K): mafic with kaolinite.

validation studies such as the study presented here have been performed using different spectral systems in different geological environments.

References

Adams, J.B., 1975. Interpretation of Visible and Near-Infrared Diffuse Reflectance Spectra of Pyroxenes and Other Rock Forming Minerals. In: Karr, C. (Ed.), Infrared and Raman Spectroscopy of Lunar and Terrestrial Materials. Academic Press, New York, pp. 91–116.

Adams, J.B., 1974. Visible and near-infrared diffuse reflectance: spectra of pyroxenes as applied to remote sensing of solid objects in the solar system. J. Geophys. Res. 79, 4829–4836.

Adams, J.B., Filice, A.L., 1967. Spectral reflectance 0.4 to 2.0 microns of silicate rock powders. J. Geophys. Res. 72, 5705–5715.

Assis, L.M., 2013. Geração de Modelo exploratório Para O minério de Ferroda Província Mineral de Carajás através Da integração de Dados Multifonte (Dissertação de Mestrado) Instituto de Geociências, Universidade de Brasília (154 p.).

Beisiegel, V.R., Bernardelli, A.L., Drummond, N.F., Ruff, A.W., Tremaine, J.W., 1973. Geologia e recursos minerais da Serra dos Carajás. Rev. Bras. Geosci. 3, 215–242.

Beukes, N.J., Gutzmer, J., Mukhopadhyay, J., 2002. The geology and genesis ofhigh-grade hematite iron ore deposits:. Australas. Inst. Min. Metall. Publ. Ser. 7, 23–29.

Bishop, J.L., Lane, M.D., Dyar, M.D., Brown, A.J., 2008. Reflectance and emission spectroscopy study of four groups of phyllosilicates: smectites, kaolinite-serpentines, chlorites and micas. Clay Miner. 43, 35–54.

Bizzi, L.A., Schobbenhaus, C., Vidotti, R.M., Gonçalves, J.H., 2003. Geologia, Tectônica E Recursos Minerais Do Brasil. Companhia de Pesquisa e Recursos Minerais – CPRM, Brasília, Brasil, p. 674.

Burns, R., 1993. Mineralogical Applications of Crystal Field Theory. second ed. Cambridge University Press, Cambridge (551 p.).

Carioca, A.C., Costa, G.M., Barrón, V., Ferreira, C.M., Torrent, J., 2011. Application of diffuse reflectance spectroscopy in the quantification of the constituents of bauxite and iron ore. Rev. Escola Min. Ouro Preto 64 (2), 199–204.

Clark, R.N., Roush, T.L., 1984. Reflectance spectroscopy-quantitative analysis techniques for remote-sensing applications. J. Geophys. Res. 89, 6329–6340.

Clark, R.N., King, T.V.V., Klejwa, M., Swayze, G.A., Vergo, N., 1990. High spectral resolution reflectance spectroscopy of minerals. J. Geophys. Res. 95, 12653–12680.

Clark, R.N., Swayze, G.A., Livo, K.E., Kokaly, R.F., Sutley, S.J., Dalton, J.B., McDougal, R.R., Gent, C.A., 2003. Imaging spectroscopy: earth and planetary remote sensing with the USGS tetracorder and expert systems. J. Geophys. Res. 108, 5-1–5-44.

Cloutis, E.A., Gaffey, M.J., Jackowski, T.L., Reed, K.L., 1986. Calibrations of phase abundance, composition, and particle size distribution for olivine-orthopyroxene mixtures from reflectance spectra. J. Geophys. Res. 91, 11641–11653.

Cordani, U.G., Tassinari, C.C.G., Teixeira, W., Basei, M.A.S., Kawashita, K., 1979. Evolução tectônica Da Amazônia Com Base Nos Dados geocronológicos. Congress. Geol. Chileno, 2, Arica, Chile, Actas. Vol. 4, pp. 137–148.

Crowley, J.K., Vergo, N., 1988. Near-infrared reflectance spectra of mixtures of kaolin-group minerals: use in clay mineral studies. Clay Clay Miner. 36, 310–316.

Cudahy, T., 1997. Pima-II Spectral Characteristics of Natural Kaolins, CSIRO/AMIRA Project P435. Sydney, Australia, CSIRO Division for Exploration and Mining Report 420R (62 p.).

Cudahy, T., Ramanaidou, E.R., 1992. Relationships between Spectral Properties and Ferric Oxides, CSIRO/AMIRA Project P243. Wembley, Australia, CSIRO Division of Exploration Geoscience Report 244R (68 p.).

Cudahy, T., and Ramanaidou, E.R.,—1997, Measurement of the hematite:goethite ratio using field visible and near-infrared reflectance spectrometry in channel iron deposits, Western Australia: Aust. J. Earth Sci., 44, p. 411–420.

Cudahy, T., Jones, M., Thomas, M., Cocks, P., Agustin, F., Caccetta, M., Rodger, A., 2009. Drill core logging of plagioclase feldspar composition and other minerals associated with Archean gold mineralization at Kambalda, Western Australia, using bidirectional thermal infrared reflectance system. Rev. Econ. Geol. 16, 223–235.

Cudahy, T., Jones, M., Thomas, M., Laukamp, C., Caccetta, M., Hewson, R., Rodger, A., Verrall, M., 2008. Next Generation Mineral Mapping:Queensland Airborne HyMap and Satellite ASTER Surveys 2006–2008. Perth, publicly Available Report P2007/364. CSIRO Exploration and Mining (http://c3dmm.csiro.au/NGMM/, 152 p.).

Curtiss, B., 1985. Evaluation of the Physical Properties of naturally Occurringiron (III) Oxyhydroxides on Rock Surfaces in Arid and Semi-Arid Regionsusing Visible and near Infrared Spectroscopy (Unpublished Ph.D. thesis) University of Washington, Seattle, WA (106 p.).

Dai, J.J., Wang, D.H., Wang, R.S., Chen, Z.H., 2013. Quantitative estimation of concentrations of dissolved rare earth elements using reflectance spectroscopy. J. Appl. Remote. Sens. 7, 073513.

Dall'Agnoll, R., de Oliveira, D.C., 2007. Oxidized, magnetite-series, rapakivi- type granites of Carajás, Brazil: implications for classification and petrogenesis of A-type granites. Lithos 93, 215–233.

Dalm, M., Buxton, M.W.N., van Ruitenbeek, F.J.A., Voncken, J.H.L., 2014. Application of near - infrared spectroscopy to sensor based sorting of a porphyry copper ore. Miner. Eng. 58 (2014), 7–16.

Dalstra, L.W.,. e, Guedes, S., 2004. Giant hydrothermal hematite deposits with Mg-Fe metasomatism: A comparison of the Carajás, Hamersley, and other iron ores. Econ. Geol. 99, 1793–1800.

Dardenne, M.A., Schobbenhaus, C., 2001. Metalogênese do Brasil. Editora Universidade De Brasília, p. 392.

DOCEGEO, 1988. Revisão litoestratigráfica Da Província Mineral de Carajás. Congresso Brasileiro de Geologia, 35th, Sociedade Brasileira de Geologia, Belém, Brazil, pp. 11–54.

Ducart, D.F., Crósta, A.P., Souza Filho, C.R., e Coniglio, J., 2006. Alteration mineralogy at the Cerro La Mina Epithermal prospect, Patagonia, Argentina: Field mapping, short-wave infrared spectroscopy, and ASTER Images. Econ. Geol. 101, 981–996.

Fernandes, R.B.A., Barrón, V., Torrent, J., Fontes, M.P.F., 2004. Quantification of iron óxides of brazilian soils using diffuse reflectance spectroscopy. Rev. Bras. Ciências Solo 28, 245–257.

Ferreira, V.N., 2014. Caracterização de formações ferríferas Bandadas através De dados De Propriedades físicas de Rocha e Sua integração Com Dados aerogeofísicos: O Estudo De Caso Do Corpo N4WS. Serra Norte – Província Mineral de Carajás. Instituto de Geociências, Universidade de Brasília Dissertação de Mestrado. (204 p.).

Figueiredo e Silva, R. C., Lobato, L.M., Rosière, C.A., Hagemann, S.H. 2011. Petrographic andgeochemical studies at giant Serra Norte iron ore deposits in the Carajás mineral province, Pará state, Brazil. Geonomos, v.19, p.198–223.

Figueiredo e Silva, R.C., Lobato, L.M., Rosière, C.A., Hagemann, S., Zucchetti, M., Baars, F.J., Andrade, I., 2008. Hydrothermal origin for the jaspilite-hosted, giant Serra Norte iron ore deposits in the Carajás mineral province, Para State, Brazil. Rev. Econ. Geol. 15, 255–290.

Gaffey, S.J., 1986a. Spectral reflectance of carbonate minerals in the visible and near-infrared (0.35 to 2.55 microns): calcite, aragonite, and dolomite. Am. Mineral. 71, 151–162.

Gaffey, S.J., 1986b. Spectral reflectance of carbonate minerals in the visible and near infra-red (0.35–2.55 \ (*mm): calcite, aragonite and dolomite. Am. Mineral. 71, 151–162.

Gibbs, A.K., Wirth, K.R., Hirata, W.K., Olszewski, e, W. J., J., 1986. Age and composition of the Grão Pará Group volcanics, Serra dos Carajás. Rev. Bras. Geosci. 16, 201–211.

Gonçalves, I.G., Petter, C.O., Machado, J.L., 2012. Quantification of hematite and goethite concentrations in kaolinusing diffuse reflectance spectroscopy: A new approach to Kubelka-Munk theory. Clay Clay Miner. 60, 473–483.

Haest, M., Cudahy, T., 2012. Quantitative mineralogy from infrared spectroscopic data. I. Validation of mineral abundance and composition algoritmos at the rocklea channel iron deposit in Western. Econ. Geol. 107 (1983), 209–228 (Retrieved from http://gsecongeo.highwire.org/content/107/2/209.short).

Harraden, C.L., Mcnulty, Brian A., Gregory, Melissa J., Lang, James R., 2013. Shortwave infrared spectral analysis of hydrothermal alteration associated with the pebble porphyry copper-gold-molybdenum deposit, Iliamna. Alaska Econ. Geol. 108, 483–494. http://dx.doi.org/10.2113/econgeo.108.3.483.

Herrmann, W., Blake, M., Doyle, M., Huston, D., Kamprad, J., Merry, N., Pontual, S., 2001. Short wavelength infrared (SWIR) spectral analysis of hydrothermal alteration zones associated with base metal sulfide deposits at Rosebery and Western Tharsis, Tasmania, and Highway-Reward, Queensland. Econ. Geol. Bull. Soc. Econ. Geol. 96 (5), 939–955.

Hillier, S., 2000. Accurate quantitative analysis of clay and other minerals in sandstones by XRD: comparison of a Rietveld and a reference intensity ratio (RIR) method and the importance of sample preparation. Clay Miner. 35, 291–302.

Hunt, G.R., 1977. Spectral signatures of particulate minerals in the visible and near-infrared. Geophysics 42, 501–513.

Hunt, G.R., Ashley, R.P., 1979. Spectra of altered rocks in the visible and near-infrared. Econ. Geol. 74, 1613–1629.

Hunt, G.R., Salisbury, J.W., 1970. Visible and near-infrared spectra of minerals and rocks, I, silicate minerals. Mod. Geol. 1, 283–300.

Hunt, G.R., Salisbury, J.W., 1971. Visible and near infrared spectra of minerals and rocks: II. carbonates. Mod. Geol. 2, 23–30.

Jiang, Z., Liu, Q., Colombo, C., Barrón, V., Torrent, J., Hu, P., 2013. Quantification of Al-goethite from diffuse reflectance spectroscopy and magnetic methods. Geophys. J. Int. 2013 http://dx.doi.org/10.1093/gji/ggt377 (Published online October 15).

Krymsky, R.S., Macambira, J.B., e Macambira, M.B.J., 2002. Geocronologia U-Pb Em zircão de Rochas vulcânicas Da Formação Carajás, Estado Do Pará [Abs.]. Simpósio Sobre Vulcanismo e Ambientes Associados, 2nd, Belém, Brazil, p. 41.

Lindenmayer, Z.G., Laux, J.H., Teixeira, J.B.G., 2001. Considerações sobre a origem das formações ferríferas da Formação Carajás, Serra dos Carajás. Rev. Bras. Geosci. 31, 21–28.

Lobato, L.M., Hagemann, S.G., R.C., Figueiredo e Silva, Thorne, W., Zucchetti, M., J., Gutzmer, 2008. Hypogene Hydrothermal Alteration Associated with BIF-Related Iron Ore Mineralization. In: Hagemann, S.G., Rosière, C.A., Gutzmer, J., Beukes, N.J. (Eds.), BIF-Related High-Grade Iron Mineralization. Reviews in Econ. Geo. Vol. 15, 107–128.

Lobato, L.M., Rosière, C.A., Figueiredo e Silva, R.C., Zucchetti, M., Baars, F.J., Seoane, J.C.S., ... Monteiro, A.M., 2005a. A mineralização Hidrotermal de Ferro Da Província Mineral de Carajás-Controle Estrutural e Contexto na evolução metalogenética Da província. In: Marini, O.J., de Queiroz, E.T., Ramos, B.W. (Eds.), Caracterização de depósitos Minerais Em Distritos Mineir, pp. 25–92.

Lobato, L.M., Figueiredo e Silva, R.C., Rosiére, C.A., Zucchetti, M., Baars, F.J., Pimentel, M.M., Rios, F.J., Seoane, J.C.S., Monteiro, A.M., 2005b. Hydrothermal origin for the iron mineralization, Carajás Province, Pará state, Brazil: iron Ore 2005. Aust. Ins. Min. Metall. Publ. Ser. 8 (2005a), 99–110 (Australia).

Macambira, J.B., 2003. O Ambiente Deposicional Da Formação Carajás e Uma Proposta de Modelo Evolutivo Para a Bacia Grão Pará. Instituto de Geociências, Universidade Estadual de Campinas, Tese de Doutorado (217 p.).

Macambira, J.B., Schrank, A., 2002. Químio-estratigrafia e evolução dos jaspilitos da Formação Carajás (PA). Rev. Bras. Geosci. 32, 567–578.

Machado, N., Lindenmayer, Z., Krogh, T.E., e Lindenmayer, D., 1991. UPb geochronology of Archean magmatism and basement reactivation in the Carajás area, Amazon shield, Brazil. Precambrian Res. 49, 329–354.

Meirelles, E.M., Hirata, W.K., Amaral, A.F., Medeiros Filho, C.A., e Gato, W.C., 1984. Geologia das folhas Carajás e Rio Verde, Província Mineral de Carajás, Estado do Pará. Congresso Brasileiro de Geologia, Rio De Janeiro, Annals. Vol. 33, pp. 2164–2174.

Meirelles, M.R., Dardenne, M.A., 1991. Vulcanismo basáltico de afinidade shonshonítica em ambiente de arco arqueano, Grupo Grão Pará, Serra dos Carajás, Pará. Resumos Expandidos Dos Anais Congresso Brasileiro de Geoquímica. Vol. 4, pp. 131–132.

Morris, R.V., Lauer, H.V., Lawson, C.A., Gibson, E.K., Nace, G.A., Stewart, C., 1985. Spectral and other physicochemcial properties of submicron powders of hematite (alpha-Fe$_0$O$_3$), maghemite (gamma-Fe$_2$O$_3$), magnetite (Fe$_3$O$_4$), goethite (alpha-FeOOH) and lepidocrocite (gamma-FeOOH). J. Geophys. Res. Solid Earth Planets 90, 3126–3144.

Mougeot, R., 1996. Estude de La Limite Archeen-Proterozoique et Des Mineralizations Au, ±U Associees. Exemples de La Region de Jacobina (Etat de Bahia, Bresil) et de Carajás (Etat de Para, Bresil). University of Montpellier II, Monpellier, France (Unpublished Ph.D. thesis).

Post, J.L., Noble, P.N., 1993. The near-infrared combination band frequencies of dioctahedral smectites, micas, and illites. Clay Clay Miner. 41, 639–644.

Resende, N.P., A.L.M., e Barbosa, 1972. Relatorio de pesquisa de minério de ferro, distrito ferrífero da Serra dos Carajás, estado do Pará. AMZA, relatório Final de Pesquisa, V. 1, Texto, 248 P, V. 2, Mapas e seções geológicas, p. 119.

Rosière, C.A., Seoane, J.C.S., Baars, F.J., Lobato, L.M., 2004. Estruturação da província de Carajás e sua influência na mineralização de ferro, PA. ADIMB, Simpósio Brasileiro de Exploração Mineral, Ouro Preto, CD-ROM.

Rosiére, C.A., Baars, F.J., Seoane, J.C.S., Lobato, L.M., da Silva, L.L., de Souza, S.R.C., Mendes, G.E., 2005. Structure and Iron Mineralisation of the Carajás Province, in: Proceedings Iron Ore 2005, P. 143–150. The Australasian Institute of Mining and Metallurgy, Melbourne.

Rosière, C.A., Baars, F.J., Seoane, J.C., Lobato, L.M., da Silva, L.L., De Souza, S.R.C., eMendes, G.E., 2006. Structure and iron mineralisation of the Carajás province. Trans. Inst. Min. Metall. 115, B126–B136.

Ross, P.-S., Bourke, A., Fresia, B., 2013. A multi-sensor logger for rock cores: methodology and preliminary results from the Matagami mining camp, Canada. Ore Geol. Rev. 53, 93–111.

Santos, J.O.S., 2003. Geotectônica dos Escudos das Guianas e Brasil-Central. In: Bizzi, L.A., Schobbenhaus, C., Vidotti, R.M., Gonçalves, J.H. (Eds.), Geologia, Tectônica E Recursos Minerais Do Brasil. Compania de Pesquisa e Recursos Minerais-CPRM, pp. 169–226.

Santos, J.S.O., Hartmann, L.A., Faria, M.S., Riker, S.R., Souza, M.M., Almeida, M.E., McNaughton, N.J., 2006. A compartimentação do Cráton Amazonas em províncias: avanços ocorridos no período 2000–2006. Simpósio de Geologia da Amazônia, 9, Sociedade Brasileira de Geologia, Belém, Brazil, Resumos Expandidos, CD ROM.

Santos, J.O.S., Hartmann, L.A., Gaudette, H.E., Groves, D.I., McNaughton, N.J., Flecher, I.R., 2000. New uderstanding of the Amazon Craton provinces, based on field work and radiogenic isotope data. Gondwana Res. 3 (4), 453–488.

Sellitto, V.M., Fernandes, R.B.A., Barrón, V., Colombo, C., 2009. Comparing two different spectroscopic techniques for the characterization of soil iron oxides: diffuse versus bi-directional reflectance. Geoderma 149, 2–9.

Senna, J.A., Souza Filho, C.R., Angélica, R.S., 2008. Characterization of clays used in the ceramic manufacturing industry by reflectance spectroscopy: an experiment in the São Simão ball-clay deposit, Brazil. Appl. Clay Sci. 41, 85–98.

Sherman, D.M. 1985. The electronic structures of Fe3 + coordination sites in iron oxides: applications to spectra, bonding, and magnetism. Phys. Chem. Miner., 12, Issue 3, pp. 161–175.

Sherman, D.M., Waite, T.D., 1985. Electronic spectra of Fe3 + oxides and oxide hydroxides in the near IR to near UV. Am. Mineral. 70, 1262–1269.

Sherman, D.M., Burns, R.G., Burns, V.M., 1982. Spectral characteristics of the iron oxides with application to the Martian Bright region mineralogy. J. Geophys. Res. 87, 169–180.

Silva, R., Hagemann, S., 2013. Hydrothermal fluid processes and evolution of the Giant Serra Norte jaspilite-hosted iron Ore deposits, Carajás Mineral Province, Brazil. Economica 108, 739–779 (Retrieved from http://gsecongeo.highwire.org/content/108/4/739.short).

Silva, G.g., Lima, M.I.C., Andrade, A.R.F., Issler, R.S., G., e Guimarães, 1974. Geologi das folhas SB-22 Araguaia e parte da SC-22 Tocantins, in Levantamento de Recursos Minerais. Projeto Radam (Departamento Nacional de Produção Mineral-SNPM e Companhia de Pesquisa e Recursos Minerais-CPRM) (143 p.).

Singer, R.B., Roush, T.L., 1985. Effects of temperature on remotely sensed mineral absorption features. J. Geophys. Res. 90, 434–444.

Sonntag, I., Laukamp, C., Hagemann, S.G., 2012. Low potassium hydrothermal alteration in low sulfidation epithermal systems as detected by IRS e XRD: an example from Co–O mine, eastern Mindanao, Philippines. Ore Geol. Rev. 45, 47–60.

Strezov, V., Ziolkowski, A., Evans, T.J., Nelson, P.F., 2010. Assessment of evolution of loss on ignition matter during heating of iron ores. J. Therm. Anal. Calorim. 100, 901–907.

Tassinari, C.C.G., 1996. O mapa geocronológico do Cráton Amazônico no Brasil: revisão dos dados isotópicos. 139p. Universidade de São Paulo, Instituto de Geociências, São Paulo. (Tese de Livre-doscência).

Tassinari, C.C.G., Macambira, M.J.B., 2004. A evolução tectônica do Cráton Amazônico. In: Mantesso-Neto, V., Bartorelli, A., Carneiro, C.D.R., Brito Nevas, B.B. (Eds.), Geologia Do Continente Sul-Americano. Evolução da Obra de Fernando Flávio Marques de Almeida, São Paulo, pp. 471–485.

Tassinari, C.C.G., Macambira, M.J.B., 1999. Geochronological provinces of the Amazonian Craton. Episodes 22, 174–182.

Tassinari, C.C.G., Bettencourt, J.S., Geraldes, M.C., Macambira, M.J.B., Lafon, J.M., 2000. The Amazonian Craton. In: Cordani, U.G., Milani, E.J., Filho, A.T., Campos, D.A. (Eds.), Tectonic Evolution of South America, pp. 41–95 (Rio de Janeiro).

Tolbert, G.E., Tremaine, J.W., Melcher, G.C., Gomes, C.B., 1971. The recently discovered Serra dos Carajás iron deposits. Northern Braz. Econ. Geol. 7, 985–994.

Townsend, T.E., 1987. Discrimination of iron alteration minerals in visible and near-infrared reflectance data. J. Geophys. Res. Solid Earth Planets 92, 1441–1454.

Van der Meer, F., 2004. Analysis of spectral absorption features in hyperspectral imagery. Int. J. Earth Observ. Geoinf. 5 (1), 55–68.

Yang, K., Huntington, J.F., Gemmel, J.B., Scott, J.M., 2011. Variation on composition and abundanceof ehite mica in hydrothermal alteration system in Hellyer, Tasmania, as reveled by infrared reflectance spectroscopy. J. Geochem. Explor. 108, 143–156.

Zhang, G.Y., Wasyliuk, K., Pan, Y.M., 2001. The characterization and quantitative analysis of clay minerals in the Athabasca Basin, Saskatchewan: application of shortwave infrared reflectance spectroscopy. Can. Mineral. 39, 1347–1363.

Zucchetti, M., 2007. Rochas máficas do Supergrupo Grão Pará e sua relação com a mineralização de ferro dos depósitos N4 e N5, Carajás, (PA) Unpublished Ph.D. thesis) Universidade Federal de Minas Gerais, Departamento de Geologia, Belo Horizonte, Brazil (125 p.).